Scholte-wave tomography for shallow-water marine sediments

Simone Kugler,[1] Thomas Bohlen,[2,*] Thomas Forbriger,[3,†] Sascha Bussat[1]
and Gerald Klein[4,‡]

[1] *Kiel University, Institute of Geosciences, Geophysics, Otto-Hahn-Platz* 1, 24118 *Kiel, Germany. E-mail:skugler@geophysik.uni-kiel.de*
[2] *Formerly Kiel University, Institute of Geosciences*
[3] *Black Forest Observatory (BFO), Institute of Geosciences, Research Facility of the Universities of Karlsruhe and Stuttgart, Heubach* 206, D-77709 *Wolfach*
[4] *Formerly IFM-Geomar, Wischhofstr.* 1-3, 24148 *Kiel, Germany*

SUMMARY

We determine the 3-D *in situ* shear-wave velocities of shallow-water marine sediments by extending the method of surface wave tomography to Scholte-wave records acquired in shallow waters. Scholte waves are excited by air-gun shots in the water column and recorded at the seafloor by ocean-bottom seismometers as well as buried geophones. Our new method comprises three steps: (1) We determine local phase-slowness values from slowness-frequency spectra calculated by a local wavefield transformation of common-receiver gathers. Areal phase-slowness maps for each frequency used as reference in the following step are obtained by interpolating the values derived from the local spectra. (2) We infer slowness residuals to those reference slowness maps by a tomographic inversion of the phase traveltimes of fundamental Scholte-wave mode. (3) The phase-slowness maps together with the residuals at different frequencies define a local dispersion curve at every location of the investigation area. From those dispersion curves we determine a model of the depth-dependency of shear-wave velocities for every location. We apply this method to a 1 km^2 investigation area in the Baltic Sea (northern Germany). The phase-slowness maps obtained in step (2) show lateral variation of up to 150 per cent. The shear-wave velocity models derived in the third step typically have very low values (60–80 m s^{-1}) in the top four meters where fine muddy sands can be observed, and values exceeding 170 m s^{-1} for the silts and sands below that level. The upper edge of glacial till with shear-wave velocities of 300–400 m s^{-1} is situated approximately 20 m below sea bottom. A sensitivity analysis reveals a maximum penetration depth of about 40 m below sea bottom, and that density may be an important parameter, best resolvable with multimode inversion.

Key words: Surface waves, Scholte waves, dispersion, tomography, inversion, shear-wave velocity, shallow marine seismics

1 INTRODUCTION

The determination of reliable 3-D models of shear-wave velocity for shallow-water marine sediments has applications in many different fields. The shear-wave velocity provides important information to characterize the sediment because it is much more sensitive to lithology variations, and less to fluid content than *P*-wave velocities are (Ayres & Theilen 1999; Hamilton 1976). The seafloor stability can be quantified by empirical relation between shear strength and shear-wave velocity of the sediment (Ayres & Theilen 1999). 3-D shear-wave velocity models thus provide important information for geotechnical applications like the foundation of offshore platforms or pipelines or the investigation of slope stability. Furthermore, in combination with *P*-wave velocity, Poisson's ratio can be inferred, which has been used to evaluate the porosity of the sediment (e.g. Hamilton 1976; Gaiser 1996).

Multicomponent acquisition and processing of marine seismic data generally benefits from the knowledge about *S*-wave velocities of the sediment. Especially in the first ten's of meters beneath the seafloor significant changes in *S*-wave velocities over small distances are commonly observed (Ewing *et al.* 1992; Stoll *et al.* 1994; Bohlen *et al.* 2004) which strongly effect processing algorithms for multicomponent seismic data like static corrections for *SH*-waves or converted *PS*-waves (Mari 1984; Muyzert 2000), wavefield separation (e.g. Schalkwijk *et al.* 2000), as well as imaging with converted waves (Tatham & Goolsbee 1984).

*Now at: TU Bergakademie Freiberg, Gustav-Zeuner-Str. 12, 09596 Freiberg, Germany.

†Also at: Geophysical Institute, University of Karlsruhe, Hertzstr. 16, D-76187 Karlsruhe, Germany.

‡Now at: develogic GmbH, Theodorstr. 42-90, Haus 4a, 22761 Hamburg, Germany.

551

Different seismic wave types can be analysed to study the shear-wave velocity structure of marine sediments. The application of interface waves provides many advantages over body shear-waves, especially in marine environments (Klein *et al.* 2005; Kugler *et al.* 2005). We analyse the dispersive interface wave travelling along the interface between water and sediment, generally called Scholte wave (e.g. Rauch 1986) or generalized Rayleigh wave. Like Rayleigh waves (travelling along an air-solid interface) and Stonley waves (near a solid–solid interface) it is a *P-SV* polarized interface wave and shows significant sensitivity to shallow shear-wave velocity. Its propagation velocity is slightly lower than that of a Rayleigh wave for small wavelengths and gradually approaches the Rayleigh-wave velocity for long wavelengths. So in the long-wavelength limit, the influence of the water-layer is negligible and the Scholte wave equals the Rayleigh wave. For smaller wavelengths it is a modified version of the Rayleigh wave that is trapped near the fluid-solid interface.

Compared to shear waves it has the advantage that it can be generated with sufficient amplitude by an air-gun source in the water column (Ritzwoller & Levshin 2002; Klein 2003; Bohlen *et al.* 2004) even for soft sediments which allows a fast data acquisition. Furthermore, because of the geometrical spreading of interface waves being 2-D, the amplitude decrease with distance is less severe. Since longer wavelength fundamental Scholte waves have a larger penetration depth than those of shorter wavelengths elastic parameters as a function of depth can be estimated by recording a broad range of frequencies.

Scholte-wave dispersion has been previously used to determine the lateral variation of shear-wave velocity of shallow-marine sediments. The analysis of local dispersion as a first step to the 2-D *S*-wave velocity model was performed by Stoll *et al.* (1994) through cross multiplication of adjacent channels of a multichannel record. Others used different local wavefield transformation methods (Allnor *et al.* 1997; Muyzert 2000; Bohlen *et al.* 2004) which have the main advantage that different Scholte-wave modes can be resolved.

In global seismology the 3-D velocity structure of the crust and upper mantle is examined very successfully by surface wave tomography since the 1970's. A 3-D shear-wave velocity model was derived, for example, by Woodhouse & Dziewonski (1984) using a waveform inversion which assumes surface waves to propagate along the great-circle avoiding the direct measurement of group and phase velocities. Global group- and phase-velocity maps have been inferred for example by Nakanishi & Anderson (1982, 1983) by measuring the dispersion of fundamental-mode surface waves. Later, as the number of digital seismic records increased, the construction of global models with higher resolution (e.g. Trampert & Woodhouse 1995) as well as regional investigations (e.g. Ritzwoller & Levshin 1998) became possible. Ray theory has played a central role in most of this research. In recent years the use of scattering theory based on the Born or Rytov approximation became popular in seismological surface-wave tomography to overcome the limitations of ray theory (e.g. Meier *et al.* 1997; Friederich 1999; Spetzler *et al.* 2002; Snieder 2002; Ritzwoller *et al.* 2002). The studies approximate the effects of surface-wave propagation in heterogeneous media to a different degree, following diverse approaches concerning single or multiple scattering and the treatment of mode coupling and conversion.

The conditions and questions found in shallow seismics, however, differ significantly from earthquake seismology restricting the range of methods that are adapted for shallow application. In shallow seismics no *a priori* reference model is available like in global seismic studies, where only relatively small perturbations to a well established reference model have to be determined. Furthermore stronger model parameter variations commonly exist, where large velocity contrasts and reversals can lead to higher mode propagation. The response-function of the receiver in shallow seismics, especially if it is deployed as an ocean-bottom seismometer on a soft seafloor, is not known without *in situ* calibration because of unknown seafloor coupling. On the other hand, shallow seismic investigations have the advantage that the positions of sources and receivers and thus the path coverage are not as restricted as in seismology. With regard to the geotechnical application in shallow marine environments a method is needed that allows a fast and robust estimate of the 3-D shear-wave velocity structure with a minimum of *a priori* information needed.

Until today the investigations of near-surface shear-wave velocities using surface waves have usually been restricted to 2-D. 3-D areal mapping in shallow land seismics was accomplished by Badal *et al.* (2004) by simply spatially interpolating between a number of 1-D phase velocity soundings over the study area. Rigorous 3-D mapping by tomography has been conducted by Dombrowski (1996) as well as Long & Kocaoglu (2001). Dombrowski recorded Rayleigh waves along many different ray paths across his study area. He determined the group velocity for each ray path by a modified wavelet transform dispersion analysis. From all group velocities he finally inferred group velocity maps using a standard traveltime tomography. He interpreted the lateral group velocity variations of the tomograms, without inverting them to shear-wave velocity models. Long & Kocaoglu used a standard multiple filter technique to measure group velocities along many different ray paths. Then they also applied a tomographic inversion method to obtain the distribution of group velocities inside that study area. The shear-wave velocity structure of the study area was determined from the group velocity dispersion curves by the inverse method outlined by Kocaoglu & Long (1993).

In this work, we analyse the phase-traveltimes of Scholte waves. We assume that the phase velocity of the Scholte mode at each point on its path equals the structural velocity as defined from the material parameters of the underlying medium. The work of Wielandt (1993), however, showed that this is only the case for plane waves.

We adapt the concept of surface wave phase-traveltime tomography to shallow-water marine environments using fundamental Scholte waves, which are excited by an air-gun source and recorded by ocean-bottom seismometers, after the approach of Bohlen *et al.* (2004) to derive fundamental mode phase slowness dispersion along straight lines in the investigation area. These phase slowness measurements are used to construct a coarse phase slowness model needed as background model in the following tomographic inversion. To linearize the problem, we assume that the Scholte wave travels along the direct path connecting source and receiver. The method basically consists of three major steps: First we construct a phase slowness background model for each frequency. In the second step we infer deviations from the background model through tomographic inversion of phase traveltimes, so we are able to construct improved phase slowness maps. The improved maps contain the areal Scholte-wave dispersion which we invert in the third step for the local 1-D shear-wave velocity variation with depth at each surface element of the area.

The paper is organised as follows: First we describe the dispersion analysis, phase traveltime tomography and inversion to 3-D shear-wave velocity. Subsequently, we present the field data and describe the data acquisition and geometry. We then infer a 1-D subsurface model and background phase-slowness maps before we describe

the application of our tomographic approach. Finally we present the resulting 3-D shear-wave velocity model.

2 METHODS

2.1 First step: Local wavefield transformation

The objective of local wavefield transformation is to identify the phase slowness of all Scholte-wave modes excited by the source for a narrowly limited subsurface region. To achieve this, the recorded wavefield is transformed from the offset-time domain into the slowness-frequency domain. Methods of wavefield transformation are described by McMechan & Yedlin (1981), Park *et al.* (1998) and Forbriger (2003a). They consist of two consecutive linear transformations. McMechan & Yedlin (1981) suggest the application of a slant-stack (p,τ-transform) followed by a 1-D Fourier transform with respect to τ. Park *et al.* (1998) and Forbriger (2003a) start with a 2-D Fourier transform and perform the summation as the second step in the frequency domain after applying an offset-dependent phase shift. Both methods generate a slowness-frequency spectrum (*p–f* spectrum), where the dispersion relation becomes apparent through the amplitude maxima. To extract local phase slowness from a recorded wavefield the offset range of the transformed seismograms has to be restricted. For this purpose successive pie-shaped phase-velocity filters can be applied to the wavefield leading to velocity-frequency spectra for each offset (Misiek 1996). Scholte waves were analysed with this method by Muyzert (2000). Bohlen *et al.* (2004) suggested the calculation of local *p–f* spectra by local slant stacking, which contains a successive offset-dependent weighting of the traces by multiplying with a Gaussian offset window before the actual transformation. However both methods suffer from the principal trade-off between the resolution in phase slowness and array aperture. This problem also exists for the spectral representation of signals in a spectrogram, where it is desirable to obtain both a high temporal and spectral resolution, but due to the uncertainty principle for the time-frequency representation of signals this is impossible there as well.

We apply the method of local slant stack described and tested in detail by Bohlen *et al.* (2004) and here give a brief summary of the procedure.

If the wavefield consists of N traces $u(x_k, t)$, recorded at the offsets x_k over the time t were $k = 1, 2, \dots, N$ denotes the shot number, the local wavefield $u_c(x_k, x_c, t)$ can be calculated by the multiplication of the original wavefield $u(x_k, t)$ with a Gaussian offset window

$$u_c(x_k, x_c, t; L) = u(x_k, t) \exp\left[-\left(\frac{x_k - x_c}{\frac{L}{2}} \right)^2 \right], \tag{1}$$

where $L/2$ denotes the distance where the window amplitude drops to $1/e$ and x_c is the centre of the Gaussian offset window. After this windowing, the local wavefield is transformed to the slowness-frequency domain through Fourier transformation

$$\tilde{u}_c(x_k, x_c, f) = \int_{-\infty}^{+\infty} u_c(x_k, x_c, t) e^{i2\pi f t} \, dt \tag{2}$$

followed by an offset-dependent phase shift $-2\pi f p x_k$ and the summation

$$\tilde{U}_c(x_c, p, f) = \sum_{k=1}^{N} \tilde{u}_c(x_k, x_c, f) e^{-i2\pi f p x_k} \tag{3}$$

over all shots k, where $\tilde{U}_c(x_c, p, f)$ is the complex *p–f* spectrum of the local wavefield for the central offset x_c.

For the calculation of local slowness-frequency spectra (*p–f* spectra) from Common Receiver Gathers (CRGs) (alternatively Common Shot Gathers (CSGs)) it is required that all receivers (shots) lie approximately on one straight line with the shot (receiver) so that the difference between two adjacent seismograms is solely caused by the medium between the two appropriate shots (receivers). For marine environments we favour the application of CRGs because it is much easier to shoot at many different air-gun source points rather than deploying a comparable number of ocean-bottom seismometers with a single shot point. In the analysis of CRGs source repeatability is an important aspect. Furthermore, the distances between the shots have to be carefully chosen depending on the slowest expected Scholte-wave velocity to avoid spatial aliasing (Bohlen *et al.* 2004; Klein *et al.* 2005).

Bohlen *et al.* (2004) have shown that the dispersion curves extracted from local *p–f* spectrum of a CRG solely depend on the medium within the analysis window. This gives us the possibility to measure the phase slowness of all excited Scholte-wave modes for discrete subsurface areas along profiles leading to a coarse background phase-slowness model, which is necessary for the tomographic inversion in the next step.

2.2 Second step: Phase traveltime tomography

In a second step we refine the coarse background model of local phase slowness by a tomographic approach. This uses data from waves that did not travel along the profiles from which local wavefield transforms were obtained.

We use a very simplified approach to surface wave propagation and assume (1) that we can separate a single Scholte mode from the rest of the wavefield in time domain, (2) that this mode can be described by a plane wave travelling along a straight line between source and receiver, and (3) that the phase velocity of the mode at each point on its path equals the structural velocity (Wielandt 1993) of the wave defined by the 1-D structure below that point.

Unfortunately reality differs from our assumptions, since: (1) interface wave propagation in shallow soil is in many cases dominated by higher modes which interfere and are coupled due to heterogeneity, and (2) the wave is generally not plane but has cylindrical symmetry in homogeneous media and undergoes severe deviations from cylindrical symmetry for laterally heterogeneous media due to wavefield scattering. We expect most severe problems to be due to the effect of lateral heterogeneity and the assumption that waves propagate along a straight line. But in contrast to global seismic studies, we are not seeking for small perturbations to a well established reference model. In shallow seismics, we believe that we can tolerate a bias of a few percent due to systematic insufficiency of our approach. If we also require the wave path and the wave curvature to depend on structure of the medium, the inverse problem would become non-linear. With our simple approach the solution is linear and straightforward. A correct wave theoretical approach that incorporates scattering (Friederich 1998) and mode coupling (Friederich 1999) would increase numerical effort by several orders of magnitude and would not be applicable without a good reference model.

Let

$$u_{lm}(t) = \int_{-\infty}^{\infty} A_{lm}(f) \, e^{i\Phi_{lm}(f)} \, e^{-2i\pi f} \, df \tag{4}$$

be the waveform of the Scholte mode that travelled from source l to receiver m. $A_{lm}(f) \in \mathbf{R}$ is then the modulus of its Fourier transform, which includes the magnitude of wave excitation and wave

attenuation along the path, and

$$\Phi_{lm}(f) = \phi_m^R(f) + \phi_l^S(f) + 2\pi f \int_{C_{lm}} p(\mathbf{x}(s), f)\, ds \qquad (5)$$

is the phase of its Fourier transform, which includes the phase delay due to finite phase slowness p and phase contributions ϕ^S and ϕ^R by the source and the receiver, respectively. C_{lm} specifies the integration path along the straight line between source and receiver and $\mathbf{x}(s)$ are the coordinates along the path. The phase slowness $p(\mathbf{x}(s), f)$ that controls wave propagation varies with location $\mathbf{x}$ and frequency f. It defines a dispersion relation at each location. The expression for the phase contribution due to wave propagation is exact in the case of plane waves propagating perpendicular to the boundaries of a band-like heterogeneity (Friederich *et al.* 1993).

For the purpose of inversion we distinguish between a mean contribution

$$\overline{p}_{lm}(f) = \frac{1}{x_{lm}} \int_{C_{lm}} p_0(\mathbf{x}(s), f)\, ds \qquad (6)$$

that is already contained in the background model $p_0(\mathbf{x}(s), f)$ and a residual contribution $\delta p(\mathbf{x}(s), f) = p(\mathbf{x}(s), f) - \overline{p}_{lm}(f)$. $x_{lm} = |\mathbf{x}_l - \mathbf{x}_m|$ is the distance between source and receiver. The background model $p_0(\mathbf{x}(s), f)$ is derived from interpolating the phase slowness of local wavefield transforms as is described later. We remove the contribution $\overline{p}_{lm}$ from the recorded data $u_{lm}^{rec}(t)$ by deconvolution. The deconvolved waveform

$$u_{lm}^{dec}(t) = \int_{-\infty}^{+\infty} \tilde{u}^{rec}(f)\, e^{-2\pi i f \overline{p}_{lm}(f) x_{lm}}\, df \qquad (7)$$

is derived by removing the phase contribution due to the background model from the Fourier transform $\tilde{u}^{rec}(f)$ of the recorded waveform. From this representation it is possible to extract the Scholte mode under investigation with a narrow taper. The bias contributed by the taper was described by Wielandt & Schenk (1993) but is ignored in our study, since it is smaller than the bias due to ignoring non-plane wave propagation. Furthermore, deconvolution is essential for determining the Fourier phase of the deconvolved signal $u_{lm}^{dec}(t)$. Phase determination is always non-unique by an additive constant of a multiple of 2π. While this happens to be a problem with $\Phi_{lm}(f)$ in particular at large offsets, the phase of the deconvolved signal can be expected to be less than 2π, if the background model is appropriate and if the mean contribution of source and receiver are removed too. For each source receiver combination we determine the phase

$$\Phi_{lm}^{dec}(f) = \mathrm{atan}\left(\frac{\mathrm{Im}(\tilde{u}_{lm}^{dec}(f))}{\mathrm{Re}(\tilde{u}_{lm}^{dec}(f))} \right) \qquad (8)$$

of the deconvolved seismogram $u_{lm}^{dec}(t)$, with $\tilde{u}_{lm}^{dec}(f)$ being the Fourier transform of $u_{lm}^{dec}(t)$. Thereby $\Phi_{lm}^{dec}(f)$ is expected to be in the range from $-\pi$ to $+\pi$. If this assumption is violated for the field data, the background model could not explain the phase values sufficiently and a phase unwrapping becomes necessary. The phase unwrapping consists of two consecutive steps and is based on the following assumptions: (1) The paths from two adjacent shots within a profile to one receiver differ only slightly, so that the phase difference of the traces should be much smaller than 2π. This equals the spatial Nyquist criterion which already has to be fulfilled for applying the local wavefield transformation when we determine the background model. (2) The background model fits the data to a similar extent for all frequencies. Therefore, the phase values belonging to two adjacent frequency samples differ only slightly. The first step unwraps from shot to shot within one profile. Therefore, we minimize the function

$$F_1(n) = \left| \Phi_{lm}^{dec}(f) - \Phi_{(l+1),m}^{dec}(f) - n2\pi \right|, n \in \mathbf{Z} \qquad (9)$$

and obtain n_{min} for which F_1 becomes minimal. The unwrapped phase can then be calculated from the original phase by

$$\hat{\Phi}_{(l+1)m}^{dec}, (f) = \Phi_{(l+1),m}^{dec}(f) - n_{min}2\pi. \qquad (10)$$

This is done consecutively for all shots l within one profile with the phase of the nearest shot to the receiver $\hat{\Phi}_{1,m}^{dec}(f) = \Phi_{1,m}^{dec}(f)$ is left unchanged. In the second step the unwrapping from frequency to frequency is realized. If we have determined the phase Φ_{lm}^{dec} for the N_f frequency samples $f_i (i = 1, \ldots, N_f)$, we minimize the function

$$F_2(n) = \left| \sum_l \hat{\Phi}_{lm}^{dec}(f_i) - \sum_l \hat{\Phi}_{lm}^{dec}(f_{i+1}) - n2\pi \right|, n \in \mathbf{Z} \qquad (11)$$

where the sum is performed over all shots within one profile and determine n_{min}. Then we apply the same phase shift $-n_{min}2\pi$ for all the shots l in the profile by

$$\hat{\Phi}_{lm}^{dec}(f_{i+1}) = \hat{\Phi}_{lm}^{dec}(f_{i+1}) - n_{min}2\pi. \qquad (12)$$

We repeat this second unwrapping for all frequency samples f_i. This two-step phase unwrapping is done independently for all profile-receiver combinations of the data set. Finally, we remove the average phase $\overline{\phi}$ for every profile and get the remaining phase

$$\phi_{lm}(f_i) = \hat{\Phi}_{lm}^{dec}(f_i) - \frac{1}{N_{shot}} \sum_l \hat{\Phi}_{lm}^{dec}(f_i) \qquad (13)$$

Unfortunately in our case no data are available to determine the receiver transfer function nor the source wavelet. We cannot distinguish between both and hence combine them to a phase contribution $\phi_P = \phi^S + \phi^R$, which is assumed to be the same for all shots along one profile P.

The $\phi_{lm}(f)$ are the data for the tomographic inversion. Unknowns are the $\delta p(\mathbf{x}(s), f)$ describing lateral variation of dispersion and the phase contribution $\delta\phi_P = \phi_P - \overline{\phi}$ due to the source and receiver. The phase slowness map $\delta p(\mathbf{x}(s), f) + p_0(\mathbf{x}(s), f)$ that characterizes the structure under investigation is then obtained by minimizing the residual

$$\phi_{lm}(f) - \delta\phi_P(f) - 2\pi f \int_{C_{lm}} \delta p(\mathbf{x}(s), f)\, ds \qquad (14)$$

in a least-squares sense with respect to $\delta\phi_P$ and $\delta p(\mathbf{x}(s), f)$ for all source and receiver combinations at once and for all frequencies, which is a linear problem.

In order to represent the tomographic model by a finite number of unknowns, we use blocks as basis functions for the parametrization of phase slowness. Thereby we divide the study area into bins with constant slowness. After discretization of the medium the integral in eq. (14) simplifies to a summation. Furthermore, if we have recorded seismograms at N_R different receiver locations, excited at N_S different source locations we can set up a linear system of equations of the form

$$\mathbf{d}^{obs} - \mathbf{G}\mathbf{m} = \mathbf{d}^{residual}, \qquad (15)$$

where $\mathbf{d}^{obs}$ is a vector containing the remaining phases $\phi_{lm}(f)$ for all source-receiver combinations at a given frequency and $\mathbf{d}^{residual}$ signifies the residuals between data and prediction. The design matrix $\mathbf{G}$ accounts for the individual ray path and $\mathbf{m}$ is the vector containing the unknowns

$$\mathbf{m}(f) = (\delta\phi_{P1}(f), \delta\phi_{P2}(f), \ldots, \delta\phi_{P(N_P+N_R)}(f),$$
$$\delta p(\mathbf{r}_1, f), \ldots, \delta p(\mathbf{r}_M, f)), \qquad (16)$$

with N_P denoting the number of profiles in the data set and M being the number of bins in the study area with the coordinates $\mathbf{r}_1, \ldots, \mathbf{r}_M$. This is done independently for each frequency f so we have dropped f in the notation.

We now search for the residuals $\mathbf{m}$ that fit the data in a least-squares sense ($|\mathbf{d}^{\mathrm{residual}}|^2 = \min$) by minimizing the objective function

$$\Psi(\mathbf{m}) = (\mathbf{d}^{\mathrm{obs}} - \mathsf{G}\mathbf{m})^{\mathrm{T}} \mathsf{C}_e (\mathbf{d}^{\mathrm{obs}} - \mathsf{G}\mathbf{m}) + \mathbf{m}^{\mathrm{T}} \mathsf{Q}\mathbf{m}, \tag{17}$$

where C_e is a diagonal matrix weighting the input data $\mathbf{d}^{\mathrm{obs}}$.

The second term of the objective function (17) describes the damping condition. With this condition *a priori* constraints for the searched model are introduced. As we will show later, our data set has regions where many ray paths intersect the bins while in other regions the data coverage is poor. This has to be balanced by the damping condition so we include a model norm constraint that takes data coverage into account. Furthermore a spatial smoothing constraint is used. This is included in the damping matrix

$$\mathsf{Q} = \mathsf{F}^{\mathrm{T}}\mathsf{F} + \mathsf{H}^{\mathrm{T}}\mathsf{H}, \tag{18}$$

which is described with more generality by Barmin *et al.* (2001). Here

$$F_{ij} = \gamma \begin{cases} 0, & \text{if } (i, j \leq N); \\ 1, & \text{if } (i, j > N) \vee (i = j); \\ -S(\mathbf{r}_{i-N}, \mathbf{r}_{j-N})/g_{i-N}, & \text{if } (i, j > N) \vee (i \neq j), \\ & \text{with } g_{i-N} = \sum_j S(\mathbf{r}_{i-N}, \mathbf{r}_{j-N}). \end{cases} \tag{19}$$

is the spatial smoothing constraint with the indices $i, j = 1, \ldots, N + M$; $N = N_P + N_R$ and S denoting the smoothing Kernel

$$S(\mathbf{r}_m, \mathbf{r}_n) = \exp\left(-\frac{|\mathbf{r}_m - \mathbf{r}_n|^2}{2\sigma^2}\right) \tag{20}$$

which includes the correlation length σ and $n, m = 1, \ldots, M$. The smoothing constraint assures that the differences between the phase slowness residual δp of a bin and the weighted sum of the phase slowness residuals of all other bins is small. The weighting is thereby dependent on the spatial distance between the bins and decreases with increasing distance like a Gaussian distribution with correlation length σ.

The model norm constraint is given by the matrix

$$H_{ij} = \begin{cases} \alpha, & \text{if } (i = j) \vee (i \leq N); \\ \beta e^{-\lambda \xi_i}, & \text{if } (i = j) \vee (i > N); \\ 0, & \text{if } (i \neq j), \end{cases} \tag{21}$$

where λ is a user-defined constant and $i, j = 1, \ldots, N + M$. The matrix H accounts for local path density ξ, that is, the number of ray paths intersecting a bin which will be described in detail later. Since the model vector $\mathbf{m}$ contains the perturbations of slowness from a background model the consideration of local path density in the model norm constraint ensures that the estimated model merges into the background model in areas of poor data coverage. The damping constants α and β specify the relative strength of damping between the model parameters of remaining phase contribution $\delta \phi_P$ due to source and receiver and the slowness residuals $\delta \mathbf{p}$. Furthermore the damping constants β and γ define the relative strength of norm constraint and smoothing to the estimated model. They control the trade-off between model amplitude and misfit. For the tomographic inversion of our data set, we find the optimal combination of damping constants by trial inversions of synthetic data sets with many different damping constants which is discussed in detail below.

We now set all partial derivatives of the objective function (17) with respect to the components of $\mathbf{m}$ to zero and obtain the matrix equation

$$\mathbf{m}^{\mathrm{est}} = (\mathsf{G}^{\mathrm{T}} \mathsf{C}_e \mathsf{G} + \mathsf{Q})^{-1} \mathsf{G}^{\mathrm{T}} \mathsf{C}_e \mathbf{d}^{\mathrm{obs}} \tag{22}$$

for the best-fitting residual phase slowness of the bins in the study area and residual phase contribution of source and receiver comprised in $\mathbf{m}^{\mathrm{est}}$.

To assess the resolution of the tomographic inversion we infer the model resolution matrix (Menke 1989). Therefore, we substitute eq. (15) with $\mathbf{d}^{\mathrm{residual}} = 0$ into expression (22) and obtain

$$\mathbf{m}^{\mathrm{est}} = \left(\mathsf{G}^{\mathrm{T}} \mathsf{C}_e \mathsf{G} + \mathsf{Q}\right)^{-1} \mathsf{G}^{\mathrm{T}} \mathsf{C}_e \mathsf{G}\mathbf{m} = \mathsf{R}\mathbf{m}, \tag{23}$$

with the symmetric model resolution matrix R. Each row of R signifies to what extend the model parameters can actually be resolved. In the ideal case of perfect resolution the resolution matrix would equal the identity matrix.

2.3 Third step: Inversion

From the phase slowness maps $p^{\mathrm{obs}}(\mathbf{r}, f)$ estimated by the described traveltime tomography we can extract local Scholte-wave dispersion curves. From this input data, we determine the local S-wave velocity $v_s(\mathbf{r}, z)$ as a function of depth z using the inversion scheme described by Bohlen *et al.* (2004). Since Scholte-wave dispersion is in principal also influenced by compressional-wave velocity and density, we will investigate the sensitivity of Scholte-wave dispersion to all seismic parameters for a single 1-D subsurface model that is representative for our study site later. The influence of seismic wave attenuation to the Scholte-wave dispersion can be neglected because the dispersion caused by moderate Q-values ($Q > 10$) is small compared to the dispersion of the Scholte wave due to structural variations of elastic parameters in the subsurface.

We describe the subsurface by k discrete layers overlying a half space. The properties of each layer are defined by shear-wave velocity v_s, compressional-wave velocity v_p, and density ρ of its top and bottom with a linear gradient in-between and the layer thickness (h) leading to the set of model parameters

$$\boldsymbol{\eta} = \left(\mathbf{h}, \mathbf{v_s}^{\mathrm{top}}, \mathbf{v_s}^{\mathrm{bot}}, \mathbf{v_p}^{\mathrm{top}}, \mathbf{v_p}^{\mathrm{bot}}, \boldsymbol{\rho}^{\mathrm{top}}, \boldsymbol{\rho}^{\mathrm{bot}}, v_s^{hs}, v_p^{hs}, \rho^{\mathrm{hs}}\right), \tag{24}$$

where the vectors of the elastic parameters have k components and $v_s^{\mathrm{hs}}, v_p^{\mathrm{hs}}, \rho^{\mathrm{hs}}$ define the elastic parameters in the half space. The starting model of the inversion is guessed by testing many different plausible models manually. The model with the best fit is then used as starting model, whereas the number of layers is the minimum number which is able to explain the measured p–f spectrum. From such a subsurface model the synthetic p–f spectrum is calculated by Wang's method (Wang 1999). The phase slowness dispersion $p^{\mathrm{mod}}(\mathbf{r}, \boldsymbol{\eta}, f_i)$ predicted by the model is obtained by automatically picking the maxima in the synthetic p–f spectrum (Bohlen *et al.* 2004). We define the relative misfit to the input data $p^{\mathrm{obs}}(\mathbf{r}, f_i)$ by the objective function:

$$\Psi(\boldsymbol{\eta}) = \frac{1}{n} \sum_{i=1}^{n} (p^{\mathrm{mod}}(\mathbf{r}, \boldsymbol{\eta}, f_i) - p^{\mathrm{obs}}(\mathbf{r}, f_i))^2, \tag{25}$$

where n denotes the number of picked frequency values. The inversion is performed without damping of the model. For the optimization of this nonlinear objective function we apply the Sequential Quadratic Programming method (function 'fmincon' of the MATLAB optimization toolbox), which is described, for example, by Boggs & Tolle (1995). The partial derivatives are derived numerically by finite differences.

3 FIELD DATA SET

3.1 Survey area

The study site is located in the Tromper Wiek, a bay situated in the northeastern part of Rügen island (northern Germany). It is open to the Baltic Sea to the northeast (Fig. 1). Tromper Wiek forms a transition area between the onshore glaciotectonically deformed deposits of Wittow, Jasmund and Schaabe on the one hand and the recent mud accumulation of the Arkona Basin on the other hand (Lemke *et al.* 1998). The recent water depth in the central part of

Tromper Wiek is about 20 m. Lemke *et al.* (1998) divide the sediment into five seismostratigraphic units on the basis of acoustical investigations and sediment core information. The uppermost till is assigned to the Weichselian glaciation and is situated approximately 20 m below sea bottom. Its upper edge is structured by late glacial channels filled with glaciolacustrine sediments of the early Baltic Ice Lake stages. These are overlain by silts or silty fine sands of freshwater origin from the final phase of the Baltic Ice Lake. In the central part of the bay the silts were covered by a younger unit of fine muddy sand, which was deposited in the Ancylus Lake. With increasing water depth to the northeast, muddy Littorina Sea sediments
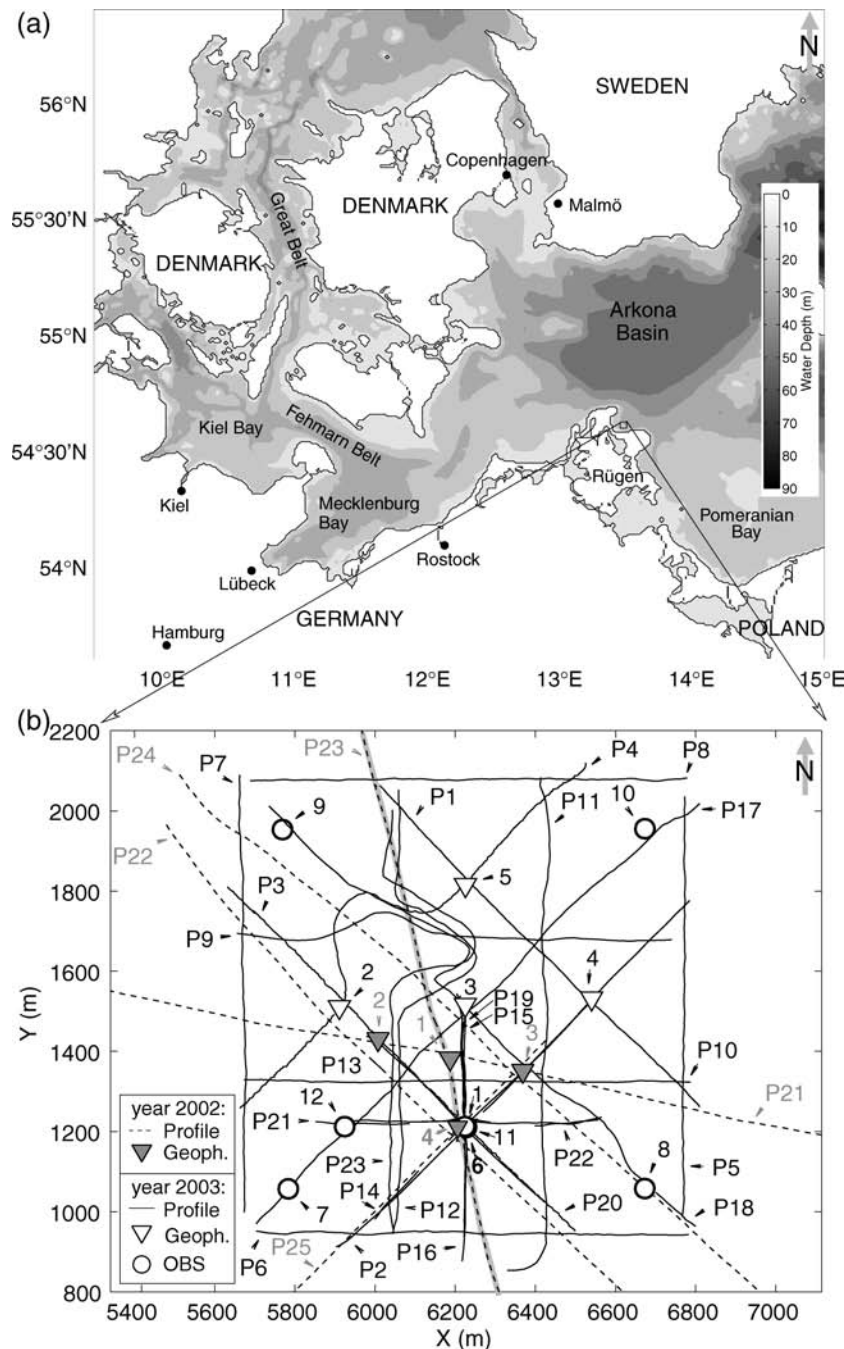
Figure 1. (a) Location of the Tromper Wiek in the Baltic Sea (north of Germany). (b) Locations of source points and receivers. The air gun was fired along the lines with shot spacings between 4 and 20 m. The circles denote the positions of OBS, the triangles of buried geophones. Records from the grey marked profile P23 (2002) recorded by geophone 4 are shown in Fig. 3.
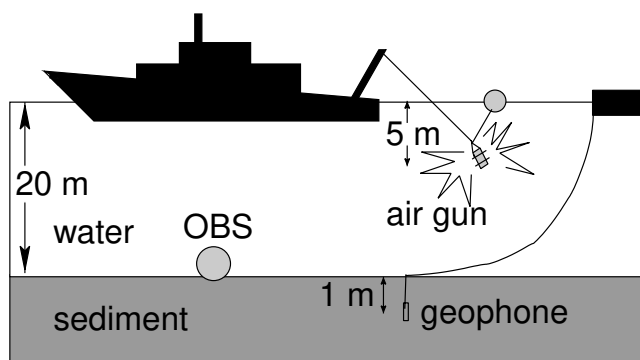
Figure 2. Acquisition parameters: Scholte waves were excited by airgun shots 5 m below sea level and recorded at the seafloor by ocean-bottom seismometers (OBS), as well as buried geophones. The water depth was about 20 m.

are observed. Our study area with the dimensions of approximately 1 km × 1 km is situated in the central part of the Tromper Wiek.

3.2 Data acquisition and geometry

For this study, we generated Scholte waves by small airgun (0.6 litre) shots in the water layer approx. 5 m below sea level and recorded them by ocean-bottom seismometers (OBS) as well as buried geophones (both with eigenfrequencies of 4 Hz) as indicated in Fig. 2. The airgun pulse had a centre frequency of approx. 35 Hz. The shots were arranged along lines with shot distances between 4 and 20 m covering the study area (Fig. 1b). Records from two surveys one year apart were gathered to a data set of 40 000 records, assuming that the elastic parameters of the sediment did not change significantly in the meantime. During the first survey in the year 2002 1250 shots were recorded by 4 receivers followed by about 3000 shots recorded by 12 receivers in the year 2003. The shot locations were measured by a differential GPS positioning system.

As an example, Fig. 3 shows a common receiver gather (CRG) recorded by the vertical component of geophone 4 (2002) for shots

along profile 23 (2002). The seismograms are normalized to their maximum amplitude to correct for amplitude variation with offset possibly caused by geometrical spreading, attenuation or source strength variation. A low-pass frequency filter is applied at 20 Hz to reduce amplitudes of body waves and guided acoustic waves. The signal-to-noise-ratio of this CRG is one of the best obtained in this survey. The records show a strong dispersed fundamental Scholte mode as well as higher mode amplitudes. The modes are normally dispersed, that is, higher frequency components propagate with smaller phase velocity. Seismograms with sufficient Scholte-wave energy for the following analysis were recorded up to 800 m offset.

4 ONE-DIMENSIONAL SUBSURFACE MODEL AND BACKGROUND PHASE SLOWNESS

In a first step towards a 3-D shear-wave velocity model we derive a first estimate of areal Scholte-wave phase slowness by local wave-field transformation along the profiles. In the middle of the study area we infer a 1-D subsurface model which was used to study the sensitivity of the Scholte-wave phase slowness to model variations as well as model resolution.

4.1 One-dimensional inversion

To get a first impression of the vertical shear-wave velocity structure in the area of investigation we inverted the fundamental mode dispersion extracted from the local *p–f* spectrum of Fig. 4. This local *p–f* spectrum was determined from the CRG of profile 23 (2002) recorded by geophone 4 (2002) (Fig. 3). The local slant stack was performed with a Gaussian offset window centred at 200 m offset with a width L of 150 m (eq. 1). The spectrum clearly exhibits the fundamental mode between 2 and 15 Hz and four higher modes in the frequency range between 5 and 22 Hz. In surface wave studies it is frequently assumed that the influence of compressional-wave velocity and density on the Scholte-wave dispersion can be neglected and therefore only shear-wave velocity and layer
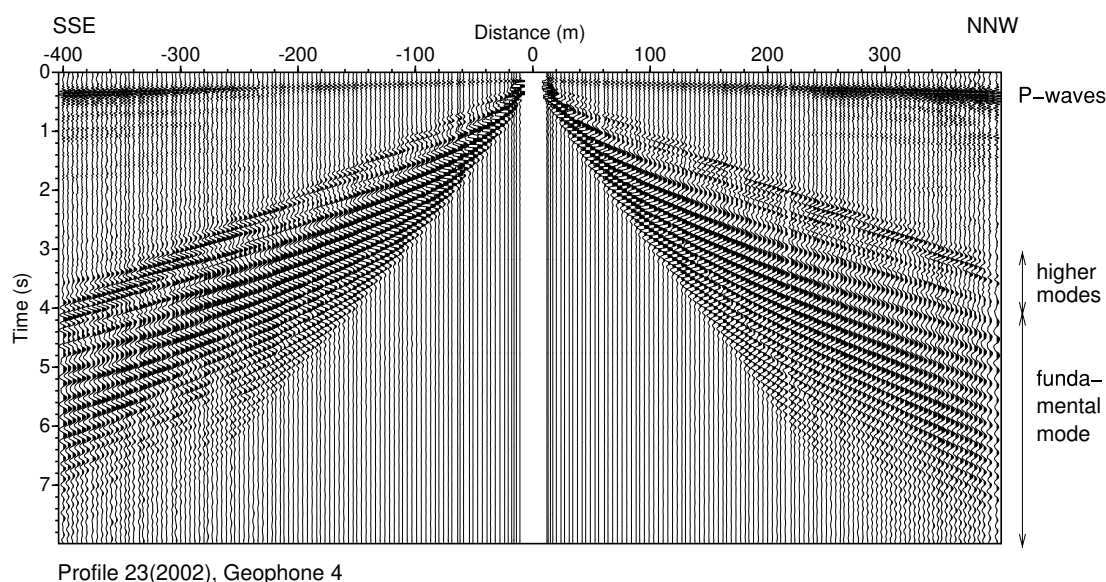
Figure 3. Common receiver gather of profile 23 (2002) recorded by the vertical component of geophone 4 (2002). The traces are normalized to their maximum amplitude and low-pass filtered below 20 Hz. A strong dispersed fundamental Scholte mode as well as faster higher modes can be observed.
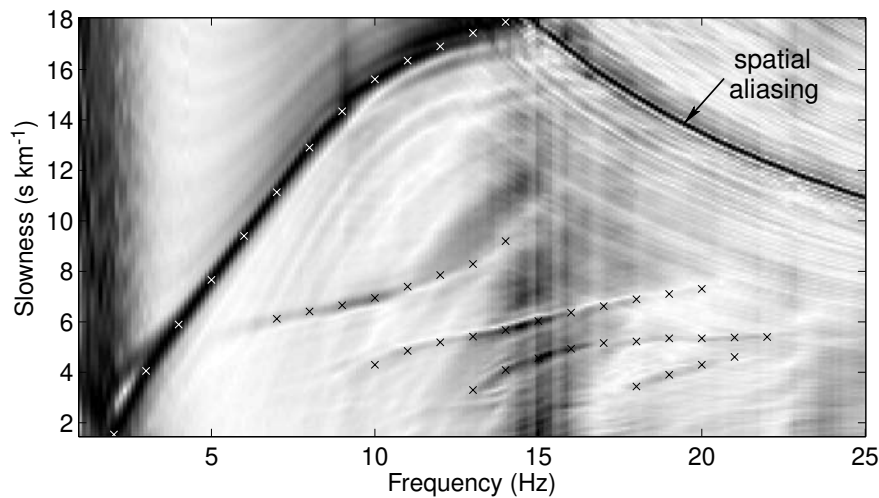
Figure 4. Local *p*–*f* spectrum calculated with the Gaussian window parameters $x_c = 200$ m and $L = 150$ m (eq. 1) from the CRG shown in Fig. 3. Besides the fundamental mode four higher modes can be distinguished. The crosses denote the picked slowness values. Spatial aliasing of the compressional waves, travelling with phase slowness smaller 0.7 s km^{-1} can be observed in the spectrum.

thickness are treated as active model parameters (e.g. Bohlen *et al.* 2004; Kugler *et al.* 2005; Park *et al.* 1999) or compressional-wave velocity and density are coupled to shear-wave velocity by some empirical relation (e.g. Herrmann & Al-Eqabi 1991). The best-fitting model inferred by inversion of only fundamental-mode dispersion is shown in Fig. 5(b) as dashed lines with the associated dispersion given in Fig. 5(a) (dashed lines). Here only shear-wave velocities and layer thickness were modified during inversion.

We have calculated sensitivity kernels with respect to shear-wave velocity, compressional-wave velocity and density by the program 'FLSPHER' (Friederich & Dalkolmo 1995). As shown for a similar model in Fig. 6, they reveal that the sensitivity of phase slowness to compressional-wave velocity variation is negligible but a significant sensitivity to density variations exists for such a model.

Thus, in this case it was not appropriate to treat density as passive inversion parameter. Moreover, it turns out that the constraints on shear-wave velocity and density are not sufficiently linearly independent. According to this, it is not possible to draw unambiguous conclusions about density variations with depth from fundamental mode data alone. We therefore include the four higher modes in the inversion. This allows sufficient resolution of density as well as shear-wave velocity.

The best-fitting model inferred by multimode inversion can be seen in Fig. 5(b) (solid lines). Fig. 5(a) shows the dispersion curves (solid lines) of this model as well as the picked slowness values of the five interpreted modes. It can be seen that a good fit between modelled and observed slowness could be achieved during multimode inversion for all analysed modes. Only the third higher mode shows slightly stronger residuals probably due to the fact, that the simple 1-D model consisting of five layers cannot fully represent the features of the real medium.

4.2 Resolution analysis

To evaluate the significance of the inverted model it is important to analyse how well the estimated model parameters are constrained by the dispersion of the five modes. Possibly there exist other combinations of model parameters that can explain the data equally well. We analyse the constrainedness of the inverted model following the

resolution analysis proposed by Forbriger (2003b). This analysis provides a local linearized estimate of constrainedness at the location of the final model in parameter space. Here we modify the resolution analysis to avoid the strong linearization. This modification, however, makes the method computationally very expensive. The procedure is as follows: At the location of the best-fitting model in the parameter space, the objective function (25) has a minimum. A variation $\Delta\eta_i$ of the *i*-th model parameter η_i will lead to an increase of the objective function (i.e. the data misfit). We then search a new minimum, by optimizing all the other model parameters by the described inversion, but holding the varied parameter η_i constant. This takes model-parameter trade-off into account. If the misfit between predicted and recorded data for this new minimum has increased by less than 10 per cent compared to the original minimum, we plot the associated model in Fig. 7 as a grey line. To limit computing time the inversion was aborted if no minimum was found after 600 iterations. We modify $\Delta\eta_i$ using nested intervals to achieve a misfit increase of 10 per cent as close as possible. The minimal interval length was 5 per cent of the best-fitting model parameter. This was done in turn for all model parameters. The black dashed line in Fig. 7 shows the original inversion result. The smaller the scatter in the suite if models, the better the parameter is constrained.

The misfit was calculated for the slowness picks of all five modes. The resolution analysis of the shear-wave velocities (Fig. 7a) shows that they are well constrained for the two shallowest layers (depth less than 5 m below seafloor). Here the maximum variations of the different models are smaller than 15 per cent. In this shallow depth region, the depth values of the layer interfaces are also well constrained. The deeper layers (between 5 and 55 m) show significant trade-off between shear-wave velocity gradients and layer thicknesses. However, the trend of shear-wave velocity variation with depth still is satisfyingly constrained. Below a depth of approximately 55 m the shear-wave velocities, as well as the layer thicknesses are barely constrained by the data.

Fig. 7(b) shows the density resolution of the inversion result. The density is not as well constrained as the shear-wave velocity. The sensitivity analysis (Fig. 6) already showed a smaller sensitivity to density compared to shear-wave velocity. The multimode inversion including the fundamental and four higher modes, however, seems to
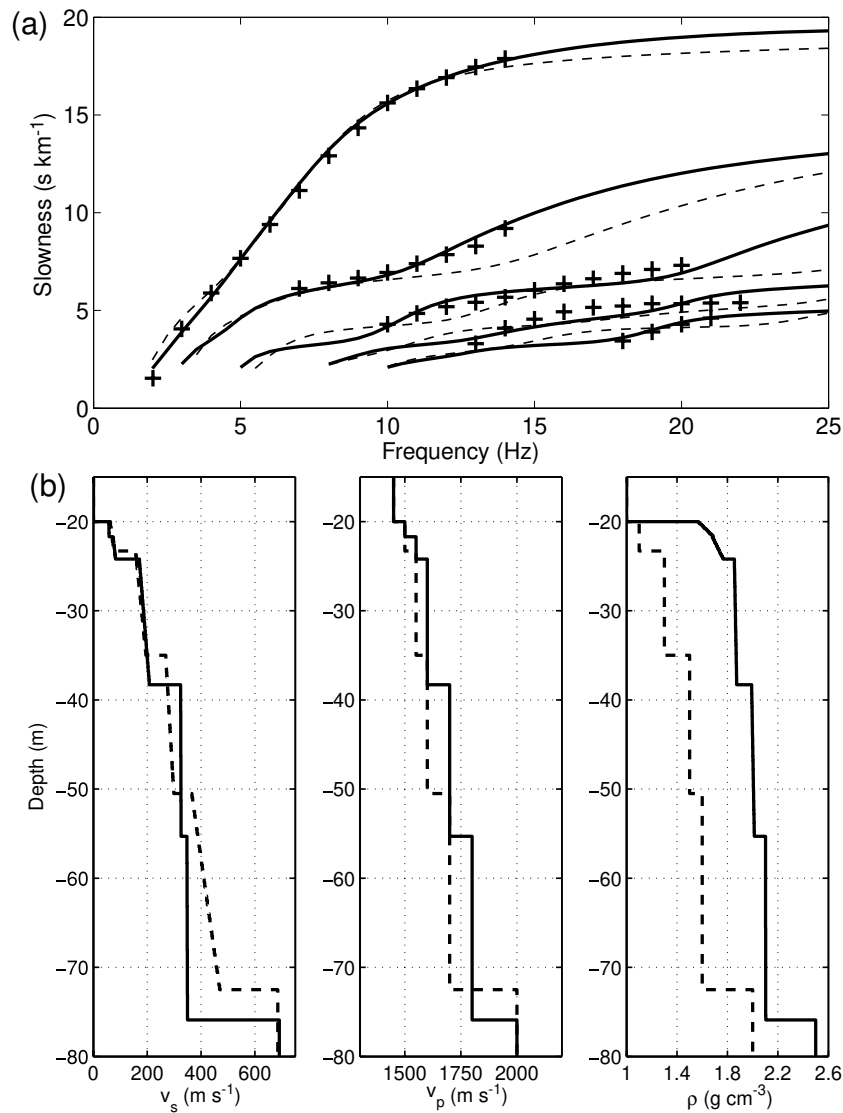
Figure 5. (a) Scholte wave dispersion curves calculated for the best-fitting models shown in (b). The dashed lines signify the dispersion for the fundamental-mode inversion model. The solid lines belong to the multimode inversion model. The picked slowness values from the local *p–f* spectrum (Fig. 4) used as input to the 1-D inversions are denoted by the crosses. Only fundamental-mode slowness picks were used for the fundamental-mode inversion, whereas all shown picks were incorporated for multimode inversion. (b) Dashed lines: best-fitting model of shear-wave velocities (left) inferred by the inversion of the picked fundamental mode slowness values. The compressional-wave velocity model (middle) and the density model (right) shown are the starting models, which were not modified during inversion. Solid lines: best-fitting model of shear-wave velocities (left) and densities (right) determined by the inversion of the picked multimode slowness values. The shown compressional-wave velocity model (middle) is the starting model and was not modified during inversion because of the poor sensitivity (Fig. 6).

be the key to obtain an improved resolution for shear-wave velocity and to resolve density at all.

### 4.3 Construction of a background phase-slowness model

The calculation of local *p–f* spectra is only valid to measure Scholte-wave slowness along the profiles. For that purpose we used a Gaussian window (eq. 1) with a width L of 100 m and moved it along the offset range of the recorded CRGs with an increment of 10 m. In Fig. 8, some examples of local *p–f* spectra of profile P23 (2002) recorded by geophone 4 for different offset values are shown. From such spectra we determine the slowness of fundamental mode Scholte wave from the amplitude maxima. The maximum frequency

of the observed Scholte wave decreases with increasing offset. Absorption and other propagation effects probably contribute to this frequency-dependent amplitude decrease. For instance in the *p–f* spectra shown in Fig. 8, the dispersion of the fundamental mode can be picked up to a frequency of 16 Hz at −200 m offset (Fig. 8a), but at −400 m offset is limited to frequencies below 7 Hz (Fig. 8c).

From all local spectra we picked the fundamental mode slowness between 2 Hz and 8 Hz with an increment of 0.5 Hz where possible. The resulting lateral slowness variation at the frequencies 3, 4, 5 and 6 Hz are shown in Fig. 9 (values in circles and diamonds). Fundamental mode slowness increases from S to N at 3 Hz (Fig. 9a) changing to an increase from SE to NW with increasing frequency. Furthermore, it can be seen that the method of local slant
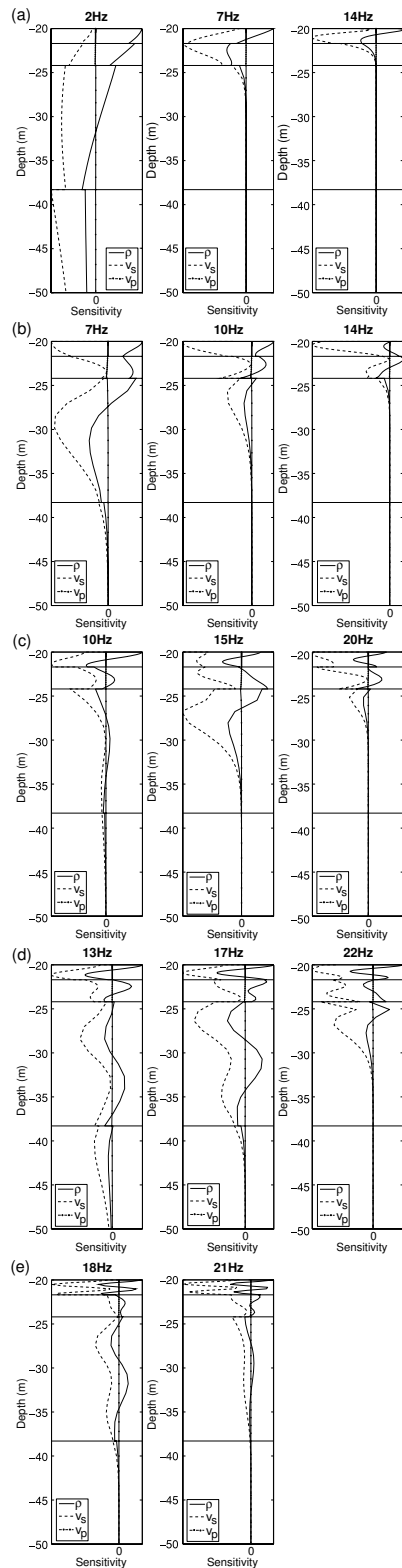
Figure 6. Sensitivity kernels of Scholte-wave modes at different frequencies for the subsurface structure given in Fig. 5 (solid lines): (a) fundamental mode, (b) to (e) next higher modes. Shown are the shear-wave velocity kernels (dashed), the density kernels (solid) and the compressional-wave velocity kernels (dashed-dotted). The horizontal black lines denote the layer boundaries. Displayed are the normalized kernels $K_n(z, f) = \frac{\partial c_n(f)}{\partial m(z)} \cdot \frac{m(z)}{c_n(f)}$ with the phase-slowness dispersion of the n-th mode $c_n(f)$ (Fig. 4), and the depth-dependent model $m(z)$ ($m \in \{v_p, v_s, \rho\}$) shown in Fig. 5 (b).
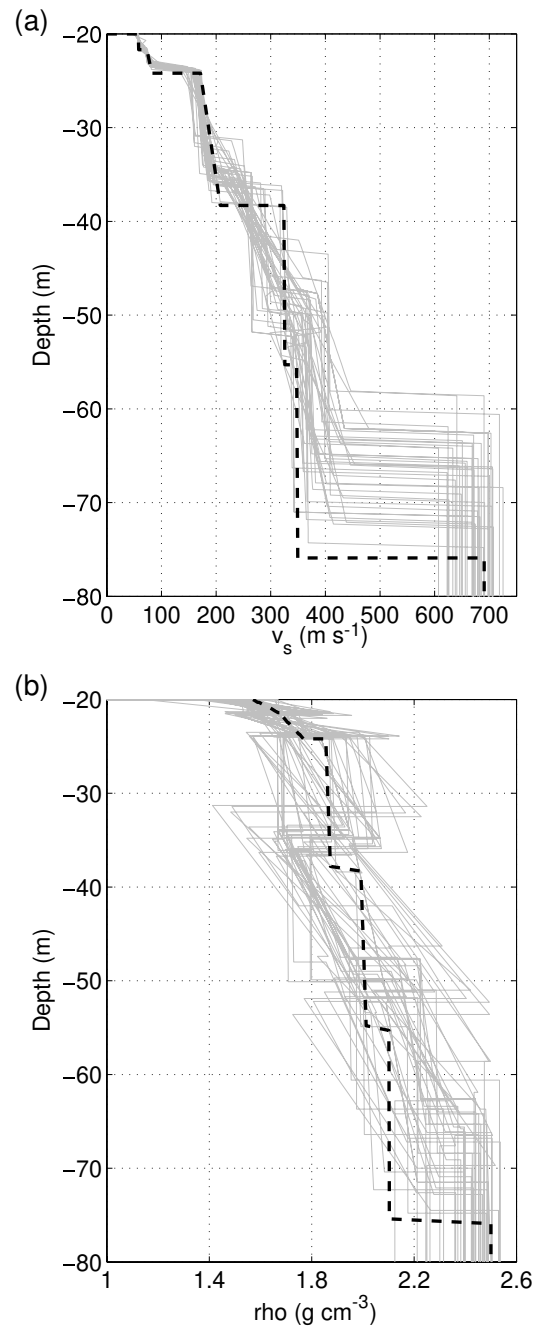
Figure 7. Results of resolution analysis for the 1-D multimode inversion of five modes. The grey lines show all the models, which lead to a misfit increase of less than 10 per cent. The black dashed line shows the best-fitting (a) shear-wave velocity model and (b) density model obtained from the inversion of the slowness picks denoted in Fig. 4. The resolution analysis takes trade-off between the model parameters shear-wave velocity, density and layer thickness into account.

stack provides consistent slowness values at the crosspoints of the profiles.

To obtain a 2-D background slowness map at each frequency from the slowness measurements of Fig. 9, we first divide the area of investigation into 40×40 m bins. Then we assign to each bin the mean of the slowness values lying within it. From the slowness values of the bins along the profiles we construct a kriging predictor (Lophaven *et al.* 2002) using a long correlation length to preserve
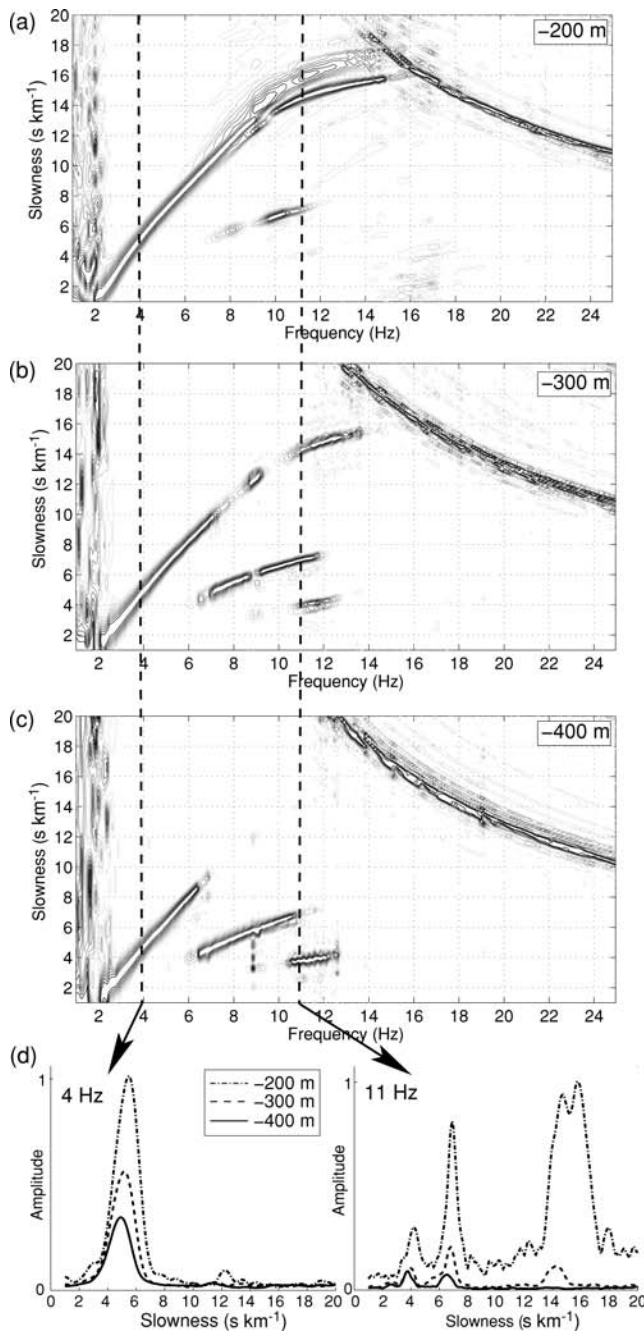
Figure 8. Local *p–f* spectra calculated from the CRG of Fig. 3 (P23, Geophone 4 (2002)) at a central offset of (a) −200 m, (b) −300 m, and (c) −400 m. The amplitudes are frequency-dependent normalized to the maximum amplitude. In (d) the unnormalized amplitudes at 4 Hz (left) and 11 Hz (right) for −200 m (dashed), −300 m (dash-dotted), and −400 m (solid) offset are plotted. Note the severe loss of fundamental mode amplitude at high frequencies with increasing offset.

only the smooth variation of the slowness. With this kriging predictor the interpolated slowness values of each bin are calculated. The result is shown in Fig. 9.

In the same way a background slowness map could be constructed for all excited higher modes. However, for the following phase traveltime tomography we have only used fundamental mode information, because data quality was not sufficient to analyse enough travelpaths for higher mode traveltime. Furthermore, the separation of
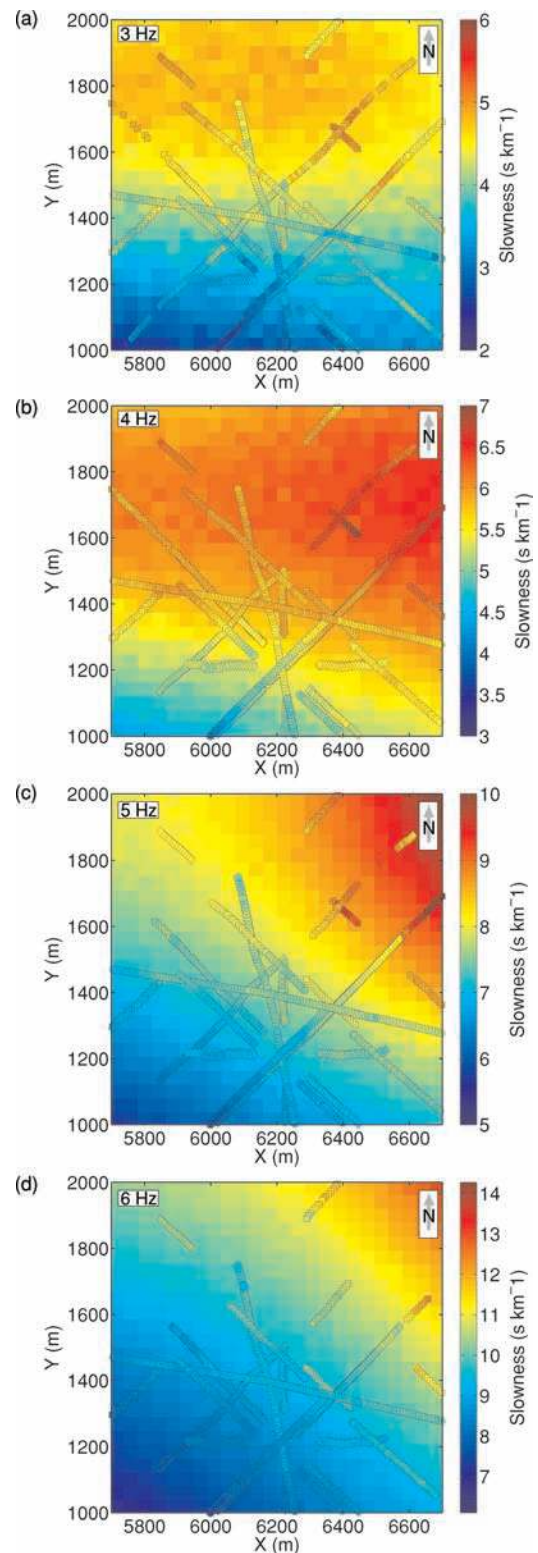
Figure 9. Lateral variation of fundamental mode phase slowness along the straight airgun profiles derived from local *p–f* spectra at the frequencies (a) 3 Hz, (b) 4 Hz, (c) 5 Hz, and (d) 6 Hz (values in circles and diamonds). The positions of circles and diamonds denote the midpoints of the Gaussian offset windows used in the calculation of local spectra from the CRGs of the year 2002 (circles) and 2003 (diamonds). The colours in the background show the background slowness model extrapolated from the slowness along the profiles. These background models only incorporate the smooth slowness trend and do not reproduce the slowness values of the spectra exactly.

modes after deconvolution is generally difficult if their slowness values are too similar. For our data set we are able to extract fundamental and first higher mode phase values from the deconvolved traces with high signal-to-noise ratio. The second to fourth higher mode, however, could not sufficiently be separated, since their slowness values are too close together.

The 2-D inferred slowness maps (Fig. 9) can now be used as a background slowness model for the application of the deconvolution (eq. 7). Before deconvolution we must interpolate the background slowness because we need to know a slowness value $p_0(\mathbf{r}, f_i)$ for each frequency sample f_i from 0 Hz to the Nyquist frequency. We use the described inversion from Scholte-wave p–f picks to shear-wave velocity model as such an interpolation method. A spline interpolation method would, however, do as well. Data input of the inversion are the background slowness values at the picked frequencies. The vector of model parameters $\boldsymbol{\eta}$ include layer thicknesses and associated shear-wave velocities for five layers and the shear-wave velocity of the half space. Above the layered sediment model, a water layer of 20 m thickness was implemented. For each bin the slowness values were inverted for a best-fitting model $\boldsymbol{\eta}(\mathbf{r})$. From those models we calculate the background slowness for every frequency needed in the deconvolution (eq. 7).

5 PHASE TRAVELTIME TOMOGRAPHY

5.1 Data preprocessing

In preparation for the tomographic inversion we extract the residual phases $\phi_{lm}(f_i)$ of fundamental Scholte wave from the deconvolved seismic traces. We will explain the procedure applied to the seismograms from CRG P23 (2002) shown in Fig. 3.

By deconvolution we remove the dispersion due to the background model $p_0(\mathbf{r}, f_i)$. Prior to the application of the deconvolution (eq. 7), it is important to extend the seismic traces to negative times since we apply a discrete Fourier transform to the data. After deconvolution the fundamental mode dispersion is almost removed as can be seen in Fig. 10, while higher mode energy was moved to

negative times. Thus the fundamental mode can be separated from the higher modes at source-receiver distances greater than approximately 50 m by muting for times smaller than -0.4 s. A sine-squared taper with a length of 0.02 s was used.

From those muted traces we obtain the residual phases by eq. (8) and apply the two-step phase unwrapping (eqs 9 to 12). The resulting phase values of the traces in Fig. 10 at the frequencies of 3 to 6 Hz are shown in Fig. 11. It can be seen, that phase differences between two adjacent shots are much smaller than 2π, so that phase unwrapping within one profile for each frequency was unambiguous. The phase differences between adjacent frequencies, however, are close to 2π at large offsets, so that phase unwrapping concerning different frequencies is problematic. After the tomographic inversion, it turns out that this 2π bias leads to 2π-jumps from frequency to frequency in the resulting instrument phase contribution $\delta\phi_P$, but is not introduced in the phase slowness residuals, because the relative phase differences within each profile for each frequency are correct.
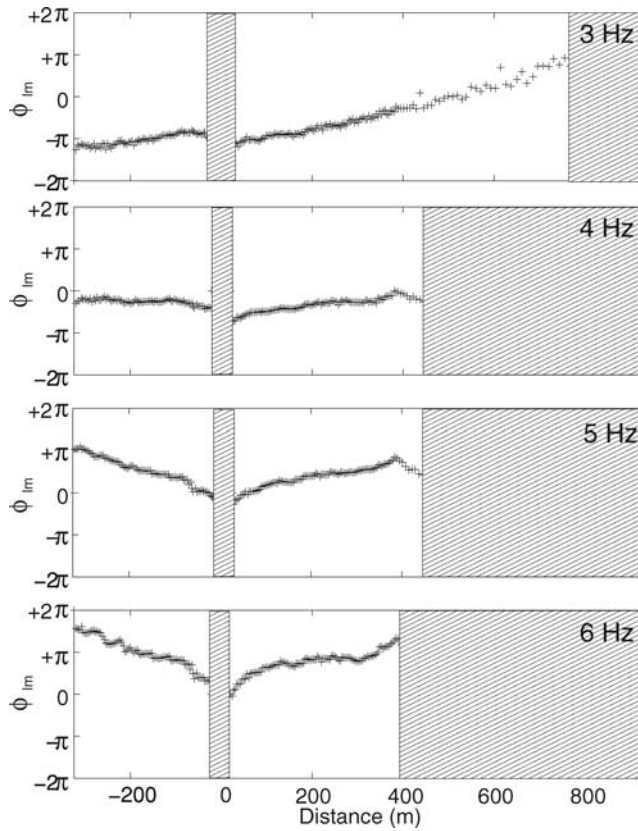
The hatched areas in Fig. 11 denote the offset regions where no reliable fundamental mode phase information could be extracted from the traces. These areas include the very small offsets (smaller 50 m) due to the increasing influence of positioning errors as the offset decreases, the superposition of higher mode energy, and near field effects. Moreover at far offsets the phase deteriorates because of the loss of amplitude with increasing offset. This latter effect is also observed in the local p–f spectra (Fig. 8). The maximum offset usable to infer fundamental mode phase values depends on the signal-to-noise ratio as well as on the frequency. From profile 23 (2002) we could use traces with source-receiver distances up to 800 m at low frequencies (3 Hz) and up to 300 m at high frequencies (6 Hz). This leads to a different number of paths intersecting the bins for each frequency (Fig. 12) in the subsequent tomographic inversion.

5.2 Model parametrization

The background-slowness model was parametrized in bins with a side length of 40 m because this is sufficient to represent this
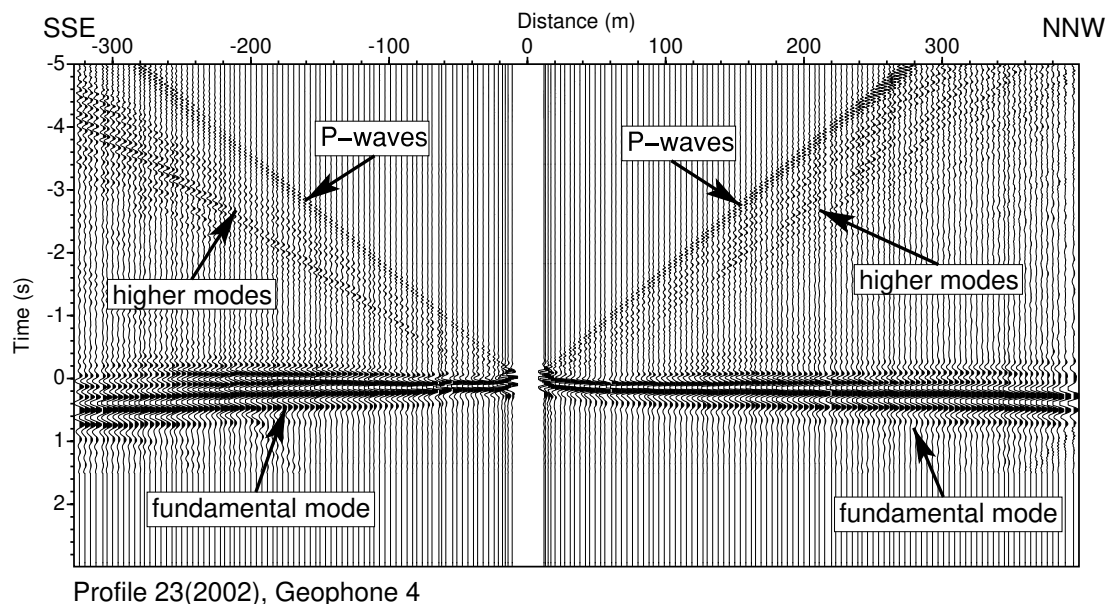
Figure 10. CRG shown in Fig. 3 after deconvolution. Amplitudes were corrected for the frequency-dependent traveltime predicted by the slowness background models shown in Fig. 9. The fundamental mode appears approximately at time zero. The dispersion contributed by the background model has been removed.

Figure 11. Phase values ϕ_{lm} (eq. 13) determined from the deconvolved seismograms shown in Fig. 10 by Fourier-transformation after muting of the higher mode energy at negative times. The hatched areas denote the offset regions where no reliable fundamental mode phase information could be extracted from the traces.

very smooth model. For the tomography we reduce the bin size since the maximum width of the first Fresnel zone of the fundamental Scholte wave with the dispersion shown in Fig. 4 is 90 m at a frequency of 2 Hz and 17 m at 14 Hz for a path length of 50 m (the minimal path length used in the tomographic inversion). We decided to use bins with a side length of 20 m for all frequencies. This is a compromise between good resolution of small scale heterogeneities and sufficient ray path coverage for each bin. The path density ξ, that is, the number of paths intersecting the 20 m × 20 m bins for which reliable fundamental mode phase values could be extracted is displayed in Fig. 12. For each bin only rays were counted, that differ in azimuth by more than two degrees. Furthermore, we only count the bins intersected by at least three paths belonging to three different profiles. This constraint is necessary to determine the instrument phase contribution $\delta\phi_P$ in the tomographic inversion uniquely. In order to keep the number of model parameters as small as possible, we have analysed the phase differences of adjacent shots and found that the initial phase contribution due to the air gun is approximately constant for all shots within one profile. We therefore use the same initial phase for all traces belonging to the same profile.

5.3 Damping and data weighting

The local path density ξ is an important part of the model norm constraint implemented in H (eq. 21). Here, the user-defined constant
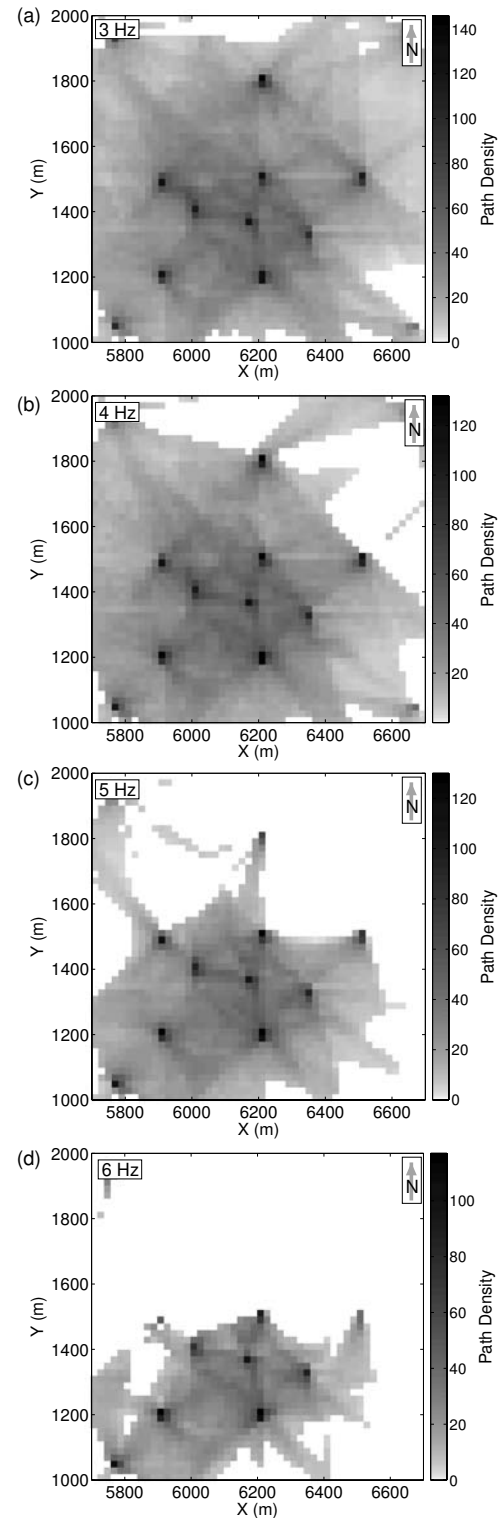
Figure 12. Number of ray paths intersecting each bin from which reliable fundamental mode phase values could be extracted at the example frequencies (a) 3 Hz, (b) 4 Hz, (c) 5 Hz, and (d) 6 Hz. Only rays are counted, that differ in azimuth by more than two degrees. If a bin is intersected by rays from less than 3 profiles the path density of the bin was set to zero. With increasing frequency the area of good ray coverage becomes smaller, because at higher frequencies only relatively short travelpaths contribute to the ray density. From longer paths no fundamental mode phase values could be extracted. Furthermore the data quality of OBS 10 and 5 (2003), which are located in the north of the study area was poor.

λ controls the strength of damping towards the background model depending on the path density. We use $\lambda = 0.08$ so if ξ is greater than about 30 paths, the resulting effective model-norm damping for this bin is less than 0.1β, with β being the damping parameter for the bins that have not been intersected at all.

To find an appropriate combination of the damping parameters α, β and γ we first apply the tomographic inversion to synthetic data sets. Therefore, we calculate a synthetic data set for a constant phase-slowness residual model ($\delta p(\mathbf{r}) = 1$ s km^{-1} for all $\mathbf{r}$). For instrument phase contributions $\delta\phi_P$ random values from a normal distribution with mean zero and variance one were used. We then determine the synthetic data set $\mathbf{d}^{\mathrm{synth}}$ by multiplying the design matrix G of the source-receiver combinations of the 4-Hz field data (path density in Fig. 12b) to this model vector. High amount of random noise was then added to the synthetic data set

$$\tilde{d}_i^{\mathrm{synth}} = d_i^{\mathrm{synth}} + \frac{\bar{d}^{\mathrm{synth}}}{10} n, i = 1, \ldots, N \qquad (26)$$

with $\bar{d}^{\mathrm{synth}} = \sum_{i=1}^{N} |d_i^{\mathrm{synth}}|$, N is the length of vector $\mathbf{d}^{\mathrm{synth}}$ and n being normally distributed random numbers with mean zero and variance one. We apply the tomographic inversion with many different combinations of damping parameters to the synthetic data set $\tilde{\mathbf{d}}^{\mathrm{synth}}$. All values of $\tilde{\mathbf{d}}^{\mathrm{synth}}$ are weighted equally within the tomographic inversion. The correlation length σ was set to 200 m for all the following tomographic inversion tests. We parametrize the model in 20 m × 20 m bins, that is, the same bin size as was used in the tomographic inversion of the field data. The resulting tomograms for six different parameter combinations are shown in Figs 13(a) to (f). To help evaluating the results of the tomographic inversion tests, we determine the rms-misfits between the model parameters used to infer the synthetic data set and the inverted parameters. For the instrument phase contribution this is denoted as $\Psi1$ and for the phase-slowness residuals as $\Psi2$ in the figures. Furthermore the rms-misfit $\Psi3$ between the noisy input phases and the phases inferred for the inverted model is shown. In the phase-slowness map of Fig. 13(a) the high overdamping ($\alpha = 2500$, $\beta = 2500$ m s^{-1}) expresses itself in strong anomalies at the positions of the receivers as well as along the profiles. A clearly underdamped map ($\alpha = 2.5$, $\beta = 2.5$ m s^{-1}) is shown in Fig. 13 b). It displays heavy artefacts in the form of speckling and stripes where high amplitudes of opposite polarity alternate. Next we choose an appropriate value for the damping of phase-slowness residuals ($\beta = 660$ m s^{-1}) and examine the effect of overdamping and underdamping the instrument phases only. This is shown in Figs 13(c) and (d) where far too high damping ($\alpha = 2500$) was chosen in (c) and far too low ($\alpha = 2.5$) in (d). It can be seen that the choice of α, though it controls the values of inferred instrument phases, only marginally effects the slowness map. The slowness maps almost only differ in the amplitudes at the positions of the receivers, especially in the north of the area where ray density is not optimal and the rays have a very limited range of azimuths. In the damping tests shown so far, no smoothing was applied (i.e. $\gamma = 0$ m s^{-1}). The effect of smoothing in addition to moderate damping can be studied in Figs 13(e) and (f). It shows that moderate smoothing ($\gamma = 1000$ m s^{-1}) reduces clearly the rms-misfit between the inverted and input phase-slowness residuals ($\Psi2$) for this example model (Fig. 13e). Stronger smoothing (Fig. 13f), however, shows a comparable effect as overdamping, that is, artefact anomalies along the profiles.

The influence of different amounts of damping was also studied at the example of a checkerboard input model. The synthetic data set was determined by the multiplication of the 4-Hz-design matrix G to the checkerboard model-parameter vector, where the phase
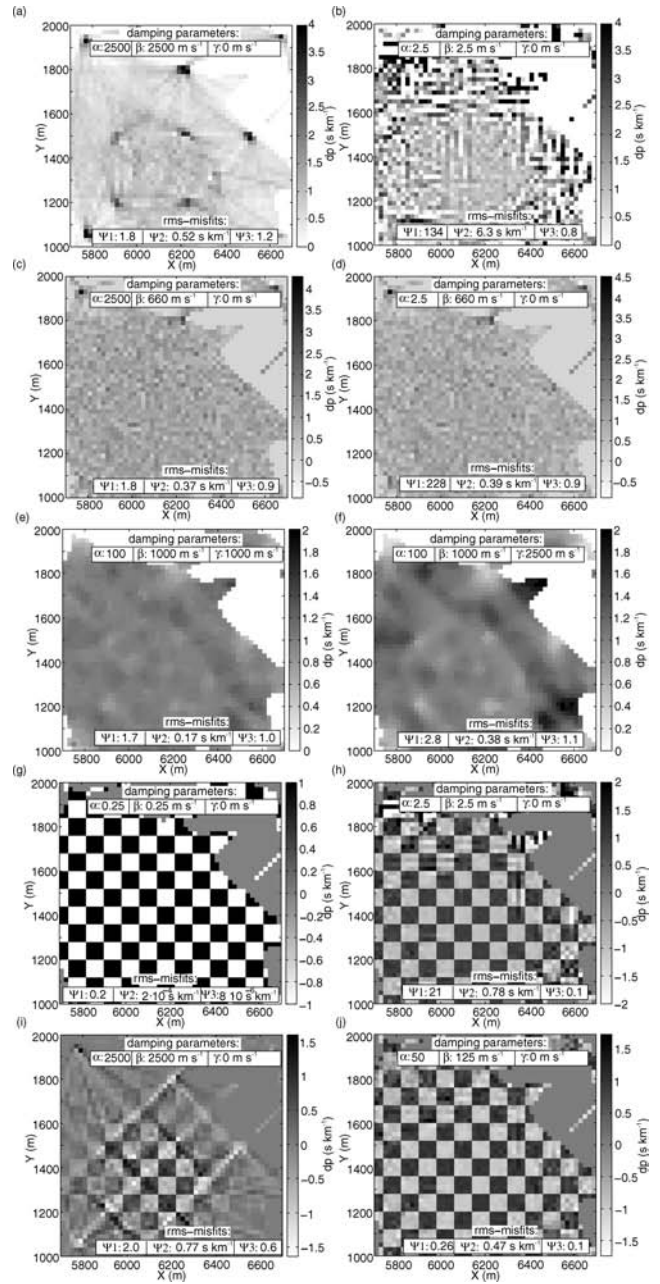
Figure 13. Phase-slowness maps for synthetic data sets reconstructed with different sets of damping parameters α, β and γ as is indicated in the boxes at the top of the maps. For all the data sets the bin size was 20 m × 20 m and $\lambda = 0.08$ and $\sigma = 200$ m were used. The synthetic data sets were calculated for a constant phase-slowness model ($\delta p = 1$ s km^{-1}) in Figs (a) to (f) and a checkerboard model (squares size: 80×80 m, $\delta p = \pm 1$ s km^{-1}) in figure (g) to (j). Random noise was added to all data sets before tomographic inversion except for figure (g). The rms-misfits between the model parameters used to infer the synthetic data sets and the inverted parameters are denoted as $\Psi1$ for the instrument phase residuals and $\Psi2$ for the phase-slowness residuals. $\Psi3$ is the rms-misfit between the noisy input traveltimes and the traveltimes inferred for the inverted model. (Note that α is given in 1/radians, $\Psi1$ and $\Psi3$ in radians). Figs (a) and (i) are highly overdamped, Figs (b) and (h) highly underdamped. In Figs (e) and (f) a smoothing constraint was applied in addition to the model-norm constraint. Only at Figs (a) and (b) amplitudes are clipped. In the shown maps the effects of too high as well as too low damping can be studied.

slowness of the model alternate between -1 and 1 s km^{-1} for 80×80 m bins. We still parametrize the model with 20×20 m bins. For a noise-free synthetic input data set the model can be perfectly reconstructed (Fig. 13g). If we add random noise to the input data set as is described in eq. (26) the effects of underdamping (Fig. 13h) and overdamping (Fig. 13i) are equivalent to the constant phase-slowness residual model. Additionally it can be seen that in areas with excellent path coverage (around the coordinates $X = 6300$ m and $Y = 1350$ m) the model can be quite well reconstructed in spite of the wrong choice of damping parameters. The inverted map for an appropriate set of damping parameters is shown in Fig. 13(j).

Based on the knowledge gained from these synthetic tests, we choose the optimal set of damping parameters for the field data in the following way. We begin with very small damping parameters α and β and no smoothing ($\gamma = 0$ m s^{-1}). Then we slowly increase α until the artefacts of underdamping as shown in Fig. 13(b) disappear. So far we have still strong anomalies at the positions of the receivers. Now we increase β until the phase-slowness residuals at the positions of the receivers are as close as possible to the residuals of the surrounding. It wasn't possible to totally eliminate those anomalies in this way, but as we have learned from the synthetic tests these only falsify the resulting model parameters of instrument phase contribution and phase-slowness residual at the positions of the receivers, leaving the rest of the model unchanged. Finally we slowly increase the smoothing parameter γ but stop before the effects of overdamping become apparent. The inferred damping parameter set for the field data is $\alpha = 0.15$, $\beta = 140$ m s^{-1} and $\gamma = 250$ m s^{-1}. These are different to the damping parameters used for the synthetic test data sets in Fig. 13 due to the different noise condition of the field data. The correlation length σ of the smoothing was set to 200 m. We decided to use the same parameter set for the tomographic inversion of all frequencies because we want to keep the model amplitudes for different frequencies comparable since we need to infer dispersion curves from the phase-slowness maps.

The weighting of the input data is implemented by the matrix $\mathbf{C}_e$ in the objective function (17). Here, we want to weight reliable phase values more than biased values. To achieve this we incorporate that the difference between the residual phases of two adjacent paths within one profile is small. Therefore, we fit a polynomial of degree 5 to the residual phases of each profile. We assume that the accurate, noise free phase values lie close to this polynomial, so we weight our input phases the more, the smaller the distance to this polynomial is.

6 RESULTS

6.1 Phase-slowness maps

The maps of phase slowness residuals derived by the tomographic inversion are shown for 3–6 Hz in Fig. 14. Here the relative deviations from the background model (Fig. 9) are displayed. If we apply the shown deviations to the background model and calculate the traveltimes of fundamental Scholte wave for all rays in the study area using the resulting model, the differences to the recorded traveltimes become minimal in a least-squares sense. It can be seen that strong anomalies of up to 20 per cent arise with a broad maximum in the north-west of the area and a minimum in the south at a frequency of 3 Hz. Anomalies become smaller with increasing frequency. At 6 Hz, for example, the slowness residual maps show anomalies as small as 100 m in diameter. The data quality of the records from the receivers in the north of the study area was, however, not sufficient,
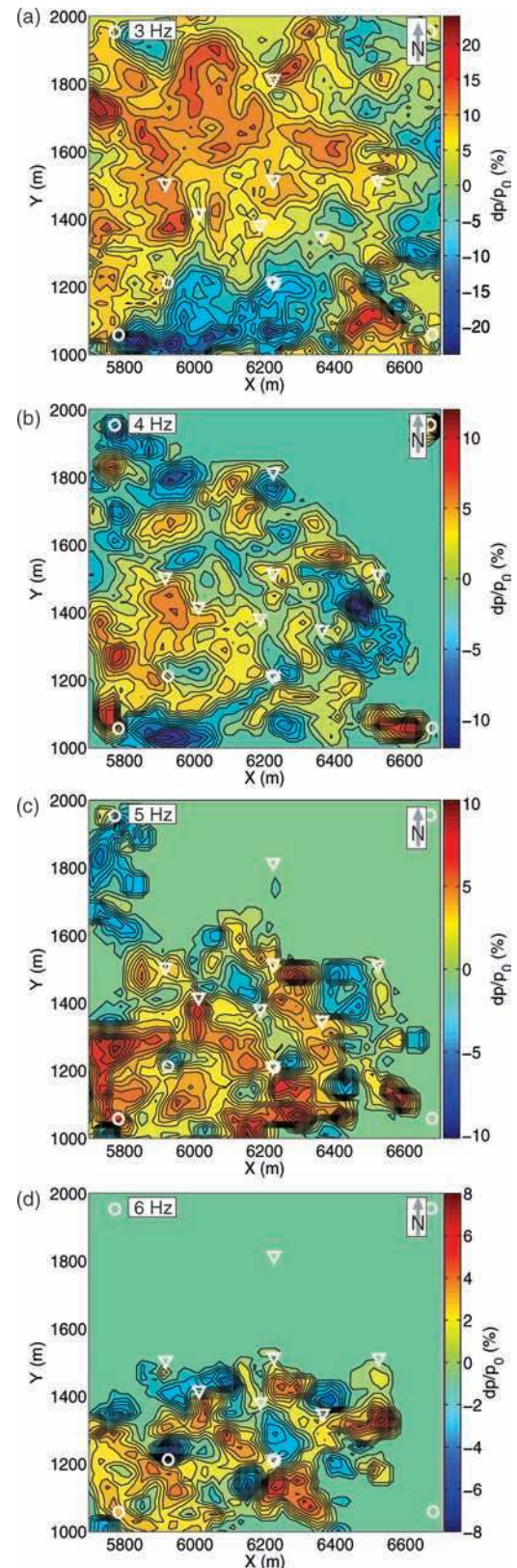
Figure 14. Maps of phase slowness residuals of fundamental Scholte mode inferred by phase traveltime tomography at the example frequencies of (a) 3 Hz, (b) 4 Hz, (c) 5 Hz, and (d) 6 Hz. The tomography extracted considerable variations to the background model of up to 20 per cent from the off-profile traveltimes. The geophone positions are denoted by the triangles and the OBSs by the circles.

so that at high frequencies the paths were only in the southern half of the area dense enough to extract information about the structural slowness. In the northern part the slowness was damped to the background model. Thus, the absence of anomalies in the northern part is caused by a lack of information from the data and has no geological reason.

## 6.2 Resolution and error analysis

We estimate the reliability of the slowness deviations obtained by tomographic inversion by analysing the model resolution matrix (eq. 23). The row values for the model parameter of phase-slowness deviation at two different bins are shown in Figs 15(a) and (b). Here the values are plotted against the coordinates of the bins to visualize the information of the resolution matrix. The peaks in the figures correspond to the particular diagonal element of the resolution matrix. A peak value of 1 would indicate that sufficient data exist to yield a unique estimate of the respective model parameter. In the middle of the study site, where the quantity as well as the number of different directions of intersecting rays are high, this is approximately the case (Fig. 15a). At the fringe of the site, however, the ray coverage decreases and the rays have very limited range of angles. Therefore, the diagonal element of the resolution matrix corresponding to the edge-bin shown in Fig. 15(b) is much smaller. The model values in this region are therefore weighted averages of the true model parameters. The off-diagonal elements of the resolution matrix indicate that this smearing occurs along the prevailing direction of travel paths in this area.

Besides the phase-slowness deviations from the background model our tomographic inversion infers the residual instrument phase contribution $\delta\phi_P$ of each profile-receiver combination. The diagonal elements of the resolution matrix of those model parameters exceed 0.98 suggesting that they can be well resolved. As an example the off-diagonal elements for profile 2(2003) recorded by OBS 2(2003) are shown in Fig. 15(c). It can be seen that the matrix has a considerable off-diagonal value for the phase-slowness deviation at the position of the OBS. This indicates trade-off between the model parameters of phase contribution of source and receiver and the model parameter of structural phase slowness at the position of the OBS.

From the resolution analysis, we can conclude that in the middle of the study site the reconstructed model is very well resolved. To the edges of the site only a blurred image of the real structure can be established. The model parameters of phase slowness residuals at the positions of the OBSs have only limited reliability because of parameter trade-off.

The discussed resolution is the theoretical resolution of the used imaging technique. The real lateral resolution of the traveltime tomography is limited by the first Fresnel-zone. It depends on the wavelength as well as on the length of the travelpath. In our tomography the length of travel paths are mainly between 50 and 400 m. This leads to a maximum width of the first Fresnel-zone for the fundamental Scholte wave with the dispersion shown in Fig. 4 at 6 Hz of 22–72 m, at 5 Hz of 27–88 m, at 4 Hz of 34–113 m and at 3 Hz of 47–156 m.

Moreover, other errors may influence the quality of the tomograms. These include incorrect positioning of sources and receivers, variation of initial phase of the source within one profile, and the interference of higher modes at small offsets. Corresponding kinds of errors for shallow land seismics were studied by O'Neill (2003), using Monte-Carlo perturbations in full wavefield *P-SV* modelling of
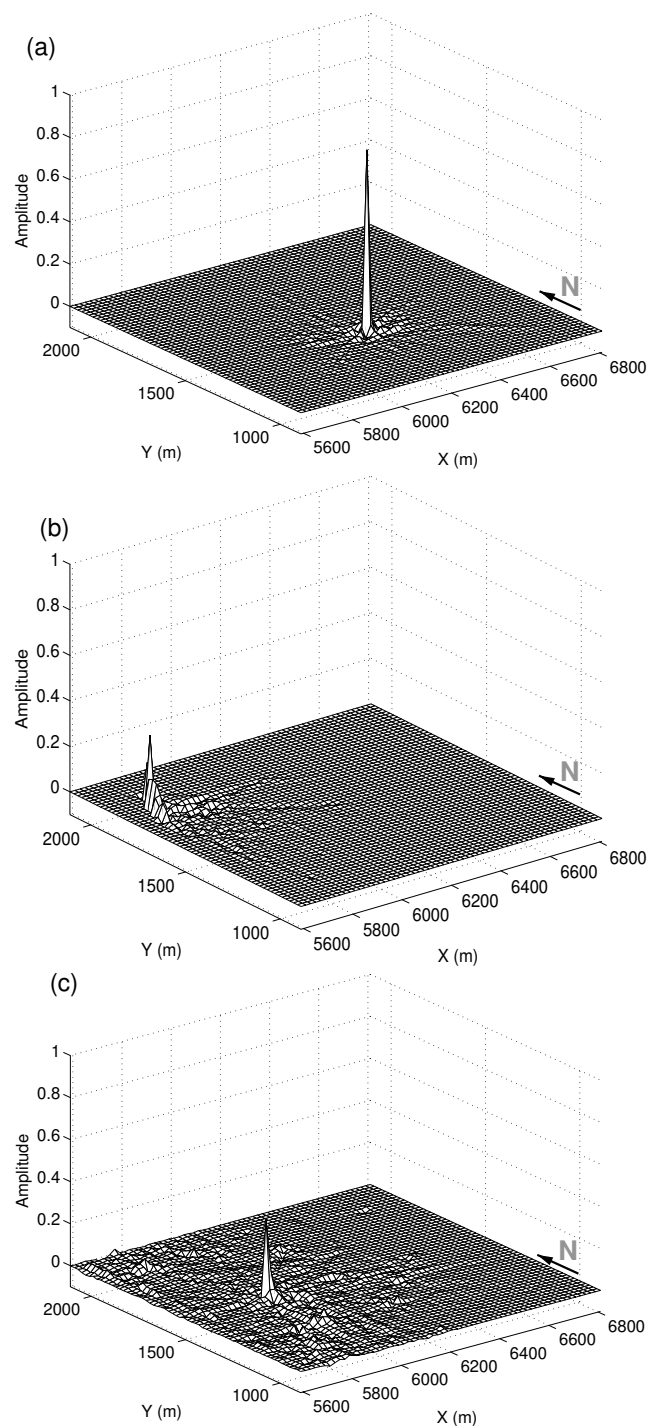
Figure 15. Row of the resolution matrix (eq. 23) at 4 Hz of the model parameter (a) phase-slowness deviation δp at $X = 6240$ m and $Y = 1420$ m, (b) phase-slowness deviation δp at $X = 5700$ m and $Y = 1940$ m, and (c) remaining instrument phase contribution $\delta\phi_P$ for profile 2 (2003) recorded by receiver 2 (2003). The row values are plotted against the coordinates of the bins. In (a) the resolution for one of the best resolved bin is displayed, whereas in (b) one of the poorest resolution can be seen. Receiver 2 in figure (c) was located at $X = 5900$ m and $Y = 1500$ m, that is, the position of the peak. The recorded profile (P2) begins at approx. $X = 6000$ m, $Y = 1000$ m and ends at $X = 6600$ m, $Y = 1600$ m.

Rayleigh waves. Trace to trace static shifts in CSGs, equivalent to initial source phase differences in CRGs, contributed most to observed dispersion errors in ideal 1-D cases. Other dominant influences were receiver positioning errors and random noise, with receiver coupling and tilt having little effect on the observed dispersion. Many of the errors observed for shallow land seismics are generally of little influence for marine settings. So are initial source phase differences negligible in marine airgun seismics and the source and receiver coupling approximately constant within one profile. Furthermore the signal-to-noise ratio of shallow marine Scholte-wave records is as far as our experience goes mostly quite high. The positioning of sources and receivers, however, is more complex and error-prone in marine seismics.

To keep the influence of those errors to a minimum each residual phase value used as input of the tomography was manually checked and outliers were excluded. Furthermore, the data weighting during tomography assures that the influence of remaining outliers is small. Strong systematic errors can exist, however, if the wave propagation in the analysed media does not satisfy the preconditions of the used traveltime tomography. This is the case if strong heterogeneities exist so that the propagating wave is not plane and scattering cannot be neglected. Then we may not specify the seismic wavefield by straight rays anymore. At our study site the heterogeneities are moderate, thus we expect these effects to be insignificant. At other study sites with strong heterogeneities the modelling of synthetic seismograms for 3-D heterogeneous media and fitting them to the recorded seismograms by waveform inversion may become necessary (Friederich 1999). This method, however, among other complications needs a good starting model which could probably be generated by the traveltime tomography.

6.3 Comparison with local spectra

By inferring local *p–f* spectra we obtained fundamental-mode phase slowness measurements along the profiles (Fig. 9). Since the background model (Fig. 9) is only a smoothed version of the readings from the local *p–f* spectra along the profiles, we expect the obtained residuals (Fig. 14) to match the residuals between *p–f* spectra and background model along profiles. We check this in Fig. 16 at a frequency of 3 Hz.
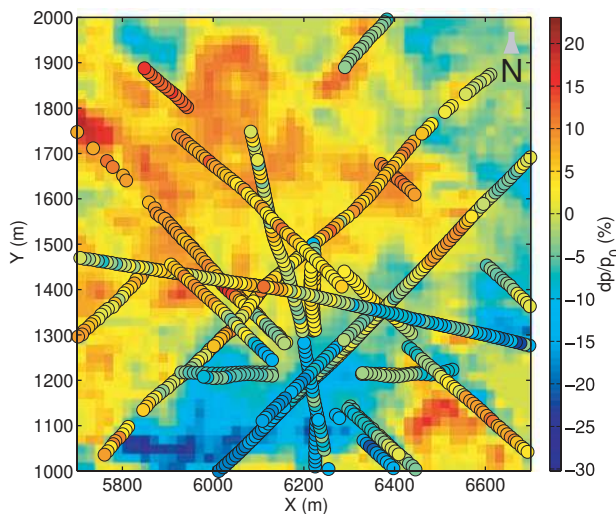
Figure 16. Comparison between the phase slowness residuals with respect to the smooth background model at 3 Hz determined by tomography and those picked from local *p–f* spectra (values in circles).

It can be seen that the slowness residuals from local spectra and those determined by tomography agree very well. This is a convincing validation of the tomograms, because the two slowness values are achieved by two different approaches (local slant stack versus traveltime tomography) on the basis of two different data sets, since the records used in the calculation of local spectra were not included in the tomography. The slowness at other frequencies also agree well. However it can be observed, that the agreement between tomographic maps and slowness residuals determined by local slant stack decreases as the path density decreases with increasing frequency. In particular at the edges of the study site the anomalies of the local slant-stack slowness residuals exceed those of the tomographic maps because of the high damping of the tomographic inversion in areas with low path density.
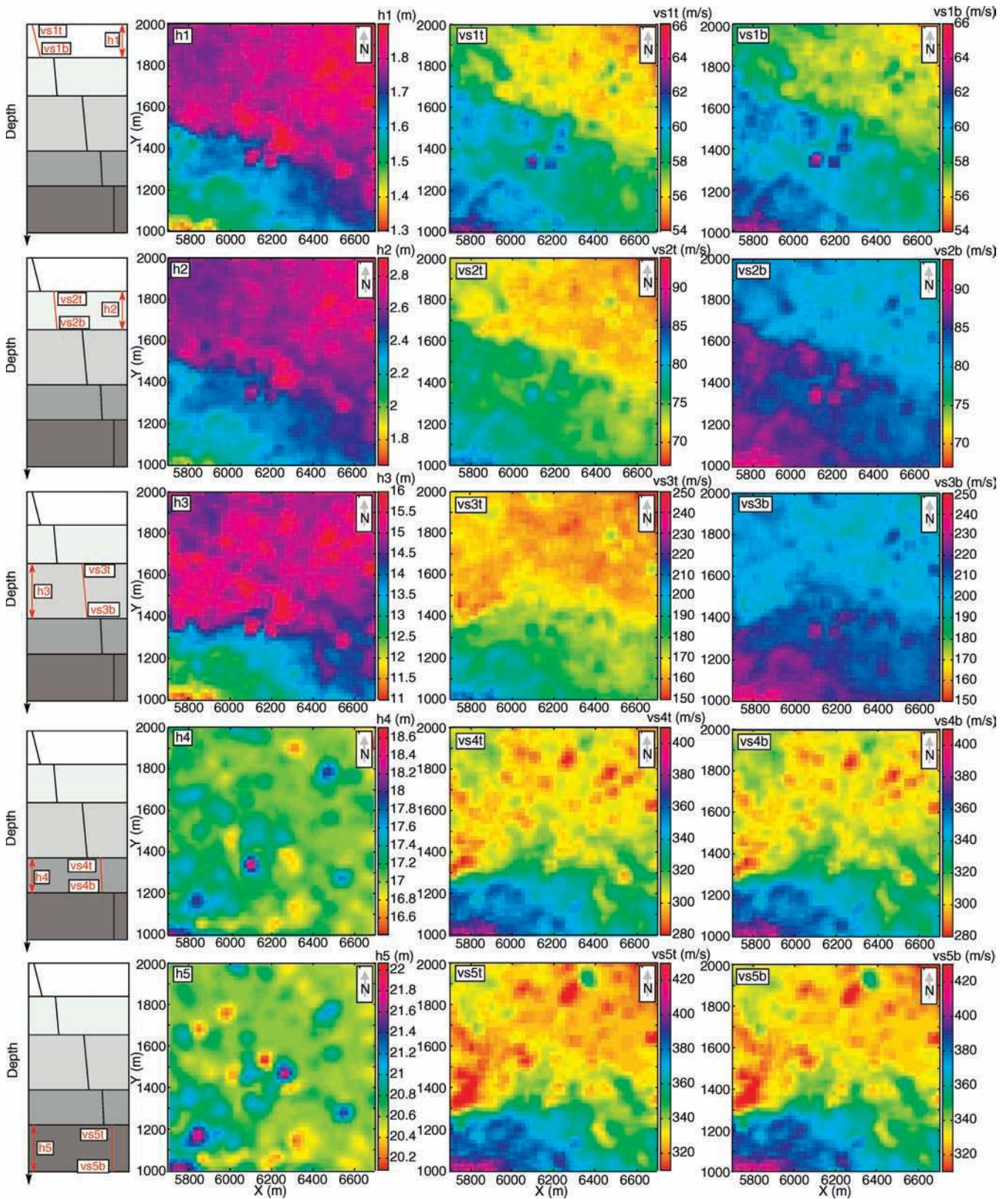
7 3-D MODEL OF SHEAR-WAVE VELOCITY

The fundamental mode dispersion at each bin from the tomographic phase slowness maps is now used to infer the final 3-D shear-wave velocity model. From the maps we obtain slowness values at frequencies from 2 to 8 Hz every 0.5 Hz. The dispersion curves of each bin were inverted independently. We started with the bin containing the location of the 1-D model shown in Fig. 5 using this model as starting model and then continue with the adjacent bins, where we used the previously inverted models from neighbouring bins as starting models. Layer thickness and shear-wave velocities of the top and bottom of each layer were active parameters, while density and compressional-wave velocity were kept constant. We have only extracted fundamental mode phase slowness information by the tomographic inversion so the density could not be included in the set of active model parameters. The density model determined by multimode inversion at the centre of the investigation area (Fig. 5b) was applied everywhere. The compressional-wave velocities which have negligible influence on Scholte wave dispersion were guessed. The inverted model consists of five layers on top of a half space. In Fig. 17 we show the inferred model parameters for the five layers.

The thickness of the two shallowest layers increase from SW to NE. The shear-wave velocities of those layers are very small (between 54 and 90 m s^{-1}) and decrease in the same direction. This is plausible since the Tromper Wiek opens to the Baltic Sea in NE-direction causing this decrease in shear-wave velocity. The third layer shows an increasing thickness from S to N with decreasing shear-wave velocities in the same direction. The thicknesses of the two deepest layers show almost no lateral variation, whereas the shear-wave velocities vary significantly with a trend of decreasing velocities from S to N. This could be caused by a buried glacial channel, but the extension of our study area is relatively small compared to the typical size of such geological structures in this region.

A vertical slice through the 3-D-shear-wave velocity cube beneath profile 23 (2002) is shown in Fig. 18(a). For a comparison we have depicted a high-resolution zero-offset section of boomer seismic data along the same profile in Fig. 18(b). The boomer source has frequencies up to 6 kHz with a centre frequency of approximately 2 kHz. The two shallowest layers showing very low shear-wave velocities are characterized by continuous, parallel, even reflections in the high-resolution seismic section of Fig. 18(b). The next deeper layer with shear-wave velocities between 150 m s^{-1} and 250 m s^{-1} extends over a depth region where many prominent reflections can be identified. This sequence is characterized by a strong shear-wave velocity gradient. The lateral variations of the reflections agree well

Figure 17. Shear-wave velocity model determined by inversion of the fundamental mode phase slowness obtained by tomography. The layer thicknesses (left), the top (middle) and bottom (right) shear-wave velocities of each layer are shown. The denotation of the model parameters is schematically displayed at the very left side of the figures. Lateral variations of layer thickness can be observed for layer one to three, whereas the layer thickness of layer four and five is almost the same for the whole study area. The shear-wave velocity gradient is the steepest for layer two and three, for the other layers the gradient is only small.
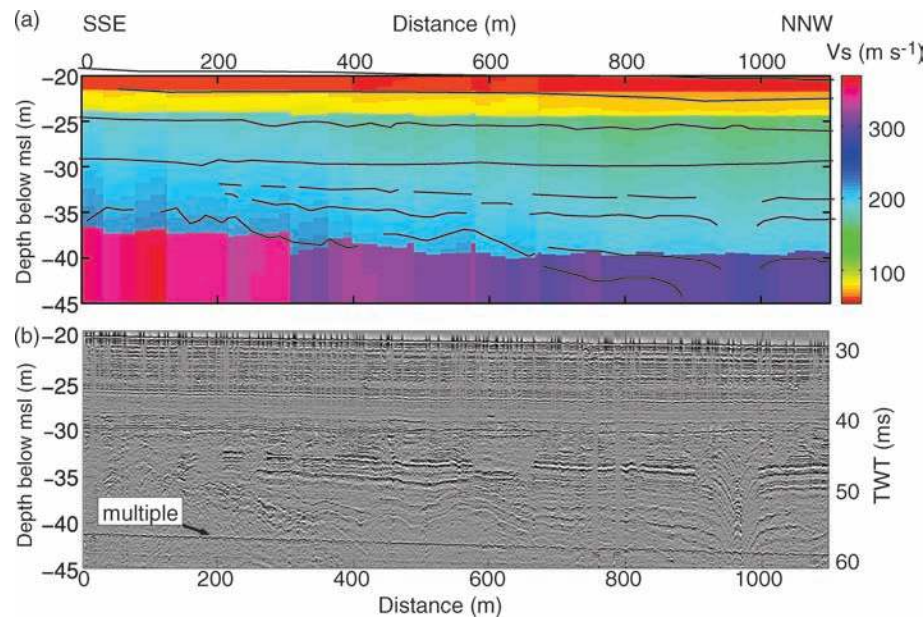
Figure 18. (a) Vertical slice through the 3-D shear-wave velocity model of Fig. 17 beneath profile 23 (2002). The black lines indicate the main reflections of the high-resolution zero-offset section of boomer seismic data along the same profile shown in (b). Depth values in (b) are estimated using a constant compressional-wave velocity of 1500 m s^{-1}.

with the lateral variation of the shear-wave velocity gradient. The layer boundary of the shear-wave velocity model at a depth of approximately 17 to 20 m can as well be observed in the high resolution seismic section. It is probably caused by the upper edge of the glacial till. The sudden increase in traveltimes of the reflections in the seismic section at 965 m distance and a depth of 12 m, however, cannot be identified in the shear-wave velocity model. The extension of this structure ($<$50 m) is probably too small to be resolved by the Scholte-wave tomography at this depth.

8 CONCLUSIONS

Scholte-wave phase-traveltime tomography is a robust and relatively fast method to estimate the 3-D shear-wave velocity structure of shallow-water marine sediments and is therefore (after calibration of shear-wave velocity to shear strength) best suited for geotechnical engineering applications in those environments.

A three-step tomographic approach is developed to infer the 3-D shear-wave velocity structure of shallow-water marine sediments using the fundamental Scholte mode excited by air guns. In the first step we construct a background model of Scholte phase slowness by slant-stacking local wavefields along common-receiver-gathers. This method yields accurate phase-velocity values along straight profiles. Phase slowness along the profiles are extrapolated to obtain a smooth background model.

In the second step phase-slowness residuals to the background model are derived by traveltime tomography. In our field data example these residuals agree well with phase-slowness residuals determined from local *p–f* spectra along the profiles. The phase-slowness residuals inferred by tomography together with the background model established a phase-slowness dispersion curve at every location of the study site.

In the third step the depth-dependency of shear-wave velocities at each location was inferred by inverting the respective dispersion curve leading to a 3-D model of shear-wave velocities. A vertical slice through this 3-D model agrees well with a high-frequency

zero-offset seismic section. Therefore, the combination of Scholte-wave traveltime tomography with areal high-frequency reflection traveltimes within a joint inversion seems to be promising.

Future work should focus on two important aspects. Higher modes should be included in the tomographic reconstruction to infer a 3-D model not only of shear-wave velocity but also of density and to enhance the vertical resolution. Furthermore, in our tomography we assume that Scholte waves travel along the direct path between source and receiver. In the case of significant lateral variations of subsurface elastic properties this assumption becomes invalid. Future tomographic applications should consider the correct ray path and account for the band limitation of the Scholte wave implying that the propagation is extended to a finite volume of space around the geometrical ray path.

ACKNOWLEDGMENTS

REFERENCES

Allnor, R., Caiti, A. & Arntsen, B., 1997. Inversion of seismic surface waves for shear wave velocities, in *Soc. of Expl. Geophys., 67th Ann. Internat. Mtg*, pp. 1921–1924, Soc. of Expl. Geophys.

Ayres, A. & Theilen, F., 1999. Relationship between P- and S-wave velocities and geological properties of near-surface sediments of the continental slope of the Barents Sea, *Geophys. Prospect.,* **47**(04), 431–441.

Badal, J., Dutta, U., Seron, F. & Biswas, N., 2004. Three-dimensional imaging of shear wave velocity in the uppermost 30 m of the soil column in Anchorage, Alaska, *Geophys. J. Int.,* **158,** 983–997.

Barmin, M.P., Ritzwoller, M.H. & Levshin, A.L., 2001. A fast and reliable method for surface wave tomography, *Pure appl. geophys.,* **158,** 1351–1375.

Boggs, P.T. & Tolle, J.W., 1995. *Sequential quadratic programming*, Acta Numerica, pp. 1–51.

Bohlen, T., Kugler, S., Klein, G. & Theilen, F., 2004. 1.5D inversion of lateral variation of Scholte-wave dispersion, *Geophysics,* **69**(02), 330–344.

Dombrowski, B., 1996. 3D-modeling, analysis and tomography of surface wave data for engineering and environmental purposes, *PhD Dissertation*, Ruhr Universität Bochum.

Ewing, J., Carter, J.A., Sutton, G.-H. & Barstow, N., 1992. Shallow water sediment properties derived from high-frequency shear and interface waves, *J. geophys. Res.,* **97**(B4), 4739–4762.

Forbriger, T., 2003a. Inversion of shallow-seismic wavefields: I. wavefield transformation, *Geophys. J. Int.,* **153**(3), 719–734.

Forbriger, T., 2003b. Inversion of shallow-seismic wavefields: II. Inferring subsurface properties from wavefield transforms, *Geophys. J. Int.,* **153**(3), 735–752.

Friederich, W., 1998. Wave-theoretical inversion of teleseismic surface waves in a regional network: phase-velocity maps and three-dimensional upper-mantle shear-wave-velocity model for southern Germany, *Geophys. J. Int.,* **132**(1), 203–225.

Friederich, W., 1999. Propagation of seismic shear and surface waves in a laterally heterogeneous mantle by multiple forward scattering, *Geophys. J. Int.,* **136,** 180–204.

Friederich, W. & Dalkolmo, J., 1995. Complete synthetic seismograms for a spherically symmetric earth by a numerical computation of the Green's function in the frequency domain, *Geophys. J. Int.,* **122,** 537–550.

Friederich, W., Wielandt, E. & Stange, S., 1993. Multiple forward scattering of surface waves: Comparison with an exact solution and born single-scattering methods, *Geophys. J. Int.,* **112,** 264–275.

Gaiser, J.E., 1996. Multicomponent Vp/Vs correlation analysis, *Geophysics,* **61**(04), 1137–1149.

Hamilton, E.L., 1976. Shear-wave velocity versus depth in marine sediments—A review, *Geophysics,* **41**(05), 985–996.

Herrmann, R. & Al-Eqabi, G., 1991. Surface wave inversion for shear wave velocity, in *Shear waves in marine sediments*, pp. 545–556, ed. by Hovem, J., Kluwer Academic Publishers.

Klein, G., 2003. Acquisition and inversion of dispersive seismic waves in shallow marine environments, *PhD Dissertation*, Universität Kiel.

Klein, G., Bohlen, T., Theilen, F., Kugler, S. & Forbriger, T., 2005. Acquisition and inversion of dispersive seismic waves in shallow marine environments, *Marine Geophysical Researches,* **2–4,** 287–315.

Kocaoglu, A.H. & Long, L.T., 1993. Tomographic inversion of Rg wave group velocities for regional near-surface velocity structure, *J. geophys. Res.,* **98**(B4), 6579–6587.

Kugler, S., Bohlen, T., Bussat, S. & Klein, G., 2005. Variability of Scholte-wave dispersion in shallow-water marine sediments, *Journal of Environmental and Engineering Geophysics, Special edition on surface waves,* **10**(2), 203–218.

Lemke, W., Endler, R., Tauber, F., Jensen, J.B. & Bennike, O., 1998. Late- and postglacial sedimentation in the Tromper Wiek northeast of Rügen (western Baltic), *Meyniana,* **50,** 155–173.

Long, L.T. & Kocaoglu, A.H., 2001. Surface-wave group-velocity tomography for shallow structures, *Journal of Environmental and Engineering Geophysics,* **6**(2), 71–81.

Lophaven, S.N., Nielsen, H.B. & Sondergaard, J., 2002. *DACE-A Matlab Kriging Toolbox, Version 2.0*, Imm-rep-2002-12, Informatics and mathematical modelling, Technical University of Denmark.

Mari, J.L., 1984. Estimation of static corrections for shear-wave profiling using the dispersion properties of Love-waves, *Geophysics,* **49**(08), 1169–1179.

McMechan, G.A. & Yedlin, M.J., 1981. Analysis of dispersive waves by wave-field transformation, *Geophysics,* **46**(06), 869–874.

Meier, T., Lebedev, S., Nolet, G. & Dahlen, F.A., 1997. Diffraction tomography using multimode surface waves, *J. geophys. Res.,* **102**(B4), 8255–8267.

Menke, W., 1989. *Geophysical Data Analysis: Discrete Inverse Theory*, Academic Press.

Misiek, R., 1996. Surface waves: Application to lithostructural interpretation of near-surface layers in the meter and decameter range, *PhD Dissertation*, Ruhr Universität Bochum.

Muyzert, E., 2000. Scholte wave velocity inversion for a near surface S-velocity model and P-S-statics, in *Soc. of Expl. Geophys., 70th Ann. Internat. Mtg,* pp. 1197–1200, Soc. of Expl. Geophys.

Nakanishi, I. & Anderson, D.L., 1982. World-wide distribution of group velocity of mantle Rayleigh waves as determined by spherical harmonic inversion, *Bull. seism. Soc. Am.,* **72,** 1185–1194.

Nakanishi, I. & Anderson, D.L., 1983. Measurements of mantle wave velocities and inversion for lateral heterogeneity and anisotropy, 1. Analysis of great circle phase velocities, *J. geophys. Res.,* **88,** 10 267–10 283.

O'Neill, A., 2003. Full-waveform reflectivity for modelling, inversion and appraisal of seismic surface wave dispersion in shallow site investigations, *PhD Dissertation*, University of Western Australia.

Park, C.B., Miller, R.D. & Xia, J., 1998. Imaging dispersion curves of surface waves on multi-channel record, in *Soc. of Expl. Geophys., 68th Ann. Internat. Mtg,* pp. 1377–1380, Soc. of Expl. Geophys.

Park, C.B., Miller, R.D. & Xia, J., 1999. Multichannel analysis of surface waves, *Geophysics,* **64**(3), 800–808.

Rauch, D., 1986. On the role of bottom interface waves in ocean seismo-acoustics: a review, in *Ocean Seismo-Acoustics Low Frequency Underwater Acoustics,* Vol. 16, pp. 623–642, eds Akal, T. & Berkson, J.

Ritzwoller, M.H. & Levshin, A.L., 1998. Eurasian surface wave tomography: Group velocities, *J. geophys. Res.,* **103**(B3), 4839–4878.

Ritzwoller, M.H., Shapiro, N.M., Barmin, M.P. & Levshin, A.L., 2002. Global surface wave diffraction tomography, *J. geophys. Res.,* **107**(B12), 2335, doi:10.1029/2002JB001777.

Ritzwoller, M.H. & Levshin, A.L., 2002. Estimating shallow shear velocities with marine multicomponent seismic data, *Geo-physics,* **67**(06), 1991–2004.

Schalkwijk, K., Wapenaar, C. & Verschuur, D., 2000. Decomposition of multicomponent ocean-bottom data: Inversion for the subbottom parameters, in *Soc. of Expl. Geophys., 70th Ann. Internat. Mtg,* pp. 1205–1208, Soc. of Expl. Geophys.

Snieder, R., 2002. *Scattering of surface waves*, pp. 562–577, Academic, San Diego, California.

Spetzler, J., Trampert, J. & Snieder, R., 2002. The effect of scattering in surface wave tomography, *Geophys. J. Int.,* **149,** 755–767.

Stoll, R.D., Bryan, G.M. & Bautista, E.O., 1994. Measuring lateral variability of sediment geoacoustic properties, *J. acoust. Soc. Am.,* **96**(1), 427–438.

Tatham, R.H. & Goolsbee, D.V., 1984. Separation of *S*-wave and *P*-wave reflections offshore western Florida, *Geophysics,* **49**(05), 493–508.

Trampert, J. & Woodhouse, J.H., 1995. Global phase velocity maps of Love and Rayleigh waves between 40 and 150 seconds, *Geophys. J. Int.,* **122,** 675–690.

Wang, R., 1999. A simple orthonormalization method for stable and efficient computations of green's functions, *Bulletin of the Seismic Society of America,* **89**(3), 733–741.

Wielandt, E., 1993. Propagation and structural interpretation of non-plane waves, *Geophys. J. Int.,* **113**(1), 45–53.

Wielandt, E. & Schenk, H., 1983. On systematic errors in phase-velocity analysis, *J. Geophys.,* **52,** 1–6.

Woodhouse, J.H. & Dziewonski, A.M., 1984. Mapping the upper manlte: Threedimensional modeling of earth structure by inversion of seismic waveforms, *J. geophys. Res.,* **89,** 5953–5986.